Award Number:
W81XWH-10-2-0101

TITLE:
Design, Fabrication, Characterization and Modeling of Integrated Functional Materials

PRINCIPAL INVESTIGATOR:
Pritish Mukherjee, Ph. D.

CONTRACTING ORGANIZATION:
University of South Florida

Tampa, FL 33620

REPORT DATE: October 2014

TYPE OF REPORT:
Annual

PREPARED FOR: U.S. Army Medical Research and Materiel Command
Fort Detrick, Maryland 21702-5012

DISTRIBUTION STATEMENT:

   Approved for public release; distribution unlimited

REPORT DOCUMENTATION PAGE

Form Approved
OMB No. 0704-0188

1. REPORT DATE	2. REPORT TYPE	3. DATES COVERED
October 2014	**Annual**	*(09-20-2013 to 09-19-2014)*

4. TITLE AND SUBTITLE	5a. CONTRACT NUMBER
Design, Fabrication, Characterization and Modeling of Integrated Functional Materials	*W81XWH-10-2-0101*
	5b. GRANT NUMBER
	5c. PROGRAM ELEMENT NUMBER

6. AUTHOR(S)	5d. PROJECT NUMBER
PI: Pritish Mukherjee, Ph. D.	
co-PIs: Hariharan Srikanth, Ph.D.; Sarath Witanachchi, Ph. D.; George Nolas, Ph. D.	**5e. TASK NUMBER**
pritish@cas.usf.edu	**5f. WORK UNIT NUMBER**

7. PERFORMING ORGANIZATION NAME(S) AND ADDRESS(ES)	8. PERFORMING ORGANIZATION REPORT NUMBER
University of South Florida 4202 East Fowler Avenue Tampa, FL 33620, USA	

9. SPONSORING / MONITORING AGENCY NAME(S) AND ADDRESS(ES)	10. SPONSOR/MONITOR'S ACRONYM(S)
U.S. Army Medical Research and Materiel Command Fort Detrick, Maryland 21702-5012	
	11. SPONSOR/MONITOR'S REPORT NUMBER(S)

12. DISTRIBUTION / AVAILABILITY STATEMENT

Approved for public release; distribution unlimited

13. SUPPLEMENTARY NOTES

14. ABSTRACT

The dynamically evolving needs of the U.S. soldier in the battlefield in response to changes in the technology of warfare and associated threats require advances in multiple areas including biomedical diagnostics, chemical sensing, communication technology, efficient power generation without increased payload, and mobile refrigeration. These technological advances are critically dependent on the development of new and currently non-existing materials. This research addresses the directed development of novel materials towards long-term needs of the United States Army. In order to address specific areas of integrated functional materials targeted towards the needs of the U.S. soldier in the field we have initiated research efforts in three main areas which are diagnostics and sensing, communication and energy, and power generation and refrigeration. The specific three independent "Tasks" that have been undertaken are:
Task I: Nanostructured materials for biomedical diagnostics and chemical sensing
Task II: Multifunctional composites for communication and energy applications
Task III: Solid-state materials for power generation and refrigeration
The specific outcome of the research activities is expected to lead to new devices/systems/composite materials useful for the USAMRMC.

15. SUBJECT TERMS

Functional materials, integrated fabrication, nanobiotechnology, multifunctional, dimensional integration, nanocomposites, sensor technology, thermoelectrics, solar cells, photovoltaics, polypeptide multilayer films, multiferroics, biomaterials, biodetection

16. SECURITY CLASSIFICATION OF:			17. LIMITATION OF ABSTRACT	18. NUMBER OF PAGES	19a. NAME OF RESPONSIBLE PERSON
					USAMRMC
a. REPORT U	**b. ABSTRACT** U	**c. THIS PAGE** U	UU	60	**19b. TELEPHONE NUMBER** *(include area code)*

Standard Form 298 (Rev. 8-98)
Prescribed by ANSI Std. Z39.18

Design, Fabrication, Characterization and Modeling of Integrated Functional Materials
(Program Director and PI: Prof. Pritish Mukherjee, Department of Physics, USF, Tampa, FL)
(co-PIs: Profs. Hariharan Srikanth, Sarath Witanachchi and George Nolas)

Table of Contents

Page

Design, Fabrication, Characterization and Modeling of Integrated Functional Materials
(Program Director and PI: Prof. Pritish Mukherjee, Department of Physics, USF, Tampa, FL)
(co-PIs: Profs. Hariharan Srikanth, Sarath Witanachchi and George Nolas)

I. Introduction

The dynamically evolving needs of the U.S. soldier in the battlefield in response to changes in the technology of warfare and associated threats require advances in multiple areas including biomedical diagnostics, chemical sensing, communication technology, efficient power generation without increased payload, and mobile refrigeration. These technological advances are critically dependent on the development of new and currently non-existing materials. This research addressed the directed development of novel materials towards long-term needs of the United States Army.

Objective:

In addition to the integration of multiple functionalities with desirable properties (thermal, electrical, magnetic, mechanical, optical, etc.), the connection to real-world applications and devices also requires the seamless integration of dimensions (nano, micro, meso, macro) leading to integrated functional materials. We have initiated this Integrated Functional Materials Project at the Physics Department at the University of South Florida (USF) geared towards precisely addressing this grand challenge of dual integration. A series of targeted projects specifically addressed a spectrum of issues relevant to the needs of the U.S. soldier.

Specific Aims:

The Physics Department at the University of South Florida is home to a unique doctoral program in Applied Physics with an affiliated industrial practicum and nationally recognized research programs in physical and chemical materials synthesis and characterization of bulk materials, thin films and nanomaterials; crystal fiber growth; fundamentals of materials manufacturing processes and computational theoretical materials physics. This research synergistically coalesced existing expertise and leverages research infrastructure at USF in novel bulk materials synthesis, thin film growth, and nanotechnology. These goals were further addressed through multidisciplinary research and new infrastructure development. The basic purpose of this project was to develop the novel science base both in the areas of multi-scale dimensional integration as well as multiple functional integration leading to previously unattained integrated functional materials.

Study Design:

In order to address specific areas of integrated functional materials targeted towards the needs of the U.S. soldier in the field we directed the research efforts in three main areas which are diagnostics and sensing, communication and energy, and power generation and refrigeration. The specific three independent "Tasks", further subdivided into seven "Projects" were:

Task I: Nanostructured materials for biomedical diagnostics and chemical sensing
       (Technical Directors.: Drs. H. Srikanth and P. Mukherjee)

Project 1	Functional magnetic fluids for biomedical applications
Project 2	Nanoporous/nano-wire structures and polymer nanotemplates for sensing and molecular manipulation
Project 3	Carbon-nanotube based sensors
Project 4	Functional materials for affecting cell proliferation and locomotion

Task II: Multifunctional composites for communication and energy applications
       (Technical Director: Dr. S. Witanachchi)

Project 5	Tunable multifunctional nano- and heterostructures for RF and microwave applications
Project 6	Flexible photonic materials for solar-based energy sources

Task III: Solid-state materials for power generation and refrigeration
       (Technical Director: Dr. G. S. Nolas)

Project 7	High-performance nanofabricated thermoelectric materials for power generation and refrigeration

II. Technical Description of Research

This research project was funded initially by Contract No.W81XWH-07-1-0708 from September 20, 2007 to September 19, 2013 (on a one-year no-cost extension) as well as by the overlapping continuation Contract No. W81XWH-10-2-0101/3349 from September 20, 2010 to September 19, 2013. The initial Contract No. W81XWH-07-1-0708 was concluded and a no-cost, two-year extension obtained for the continuation grant W81XWH-10-2-0101/3349 until September 19, 2015. The past year was therefore Year 4 of the continuation.

The following discussion provides salient technical details of research performed during the past year on the remaining sub-tasks.

Nanostructured materials for biomedical diagnostics and chemical sensing

The goal of this project is to synthesize and characterize functional magnetic nanomaterials for high-performance sensor and biomedical applications. In continued work during this year, we have successfully synthesized and characterized iron oxide nanoparticles of different sizes and shapes (sphere, cube, and octopod), core/shell $Fe/\gamma Fe_2O_3$ nanoparticles with tunable sizes, exchange-coupled FeO/Fe_3O_4 nanoparticles with tunable sizes and shapes (sphere, cube and octopod), and FeCo nanowires with tunable dimensions. Magneto-inductive heating measurements performed on these nanostructures reveal the importance of using shape- and size-variant nanostructures for advanced hyperthermia. We have also developed a novel high-aspect ratio nanostructure composed of carbon nanotubes filled with nickel ferrite and core/shell iron/iron oxide nanoparticles for biomedical and microwave device applications. A new sensor using a soft ferromagnetic microwire and an optical technique for microwave energy sensing has been developed. A novel class of magnetic sensors using the longitudinally excited magneto-inductance (LEMI) effect and multiple soft ferromagnetic microwires has been developed. An ultrasensitive biosensor using the magneto-reactance effect of a soft ferromagnetic ribbon with a nanohole-patterned surface has been developed for detection and qualification of cancer cells and anticancer drugs tagged to functionalized magnetic nanoparticles. A graduate student Mr. Jagannath Devkota received support and worked on this project. In addition, undergraduate students, Mr. Luis Martinez Milian and Ms. Izzi Berman, graduate students, Ms. Kristen Stojak and Ms. Zohreh Nemati Porshokouh, Postdoctoral Researcher Dr. Hafsa Khurshid, Visiting Postdoctoral Associate Dr. Javier Alonso and Research Assistant Professor Dr. Manh-Huong Phan were key contributors to the project. A summary of our research activities and major results in the year of 2013-2014 is highlighted below:

A. Inductive heating (hyperthermia) studies on novel magnetic nanostructures

Magnetic nanostructures have received growing interest in the scientific community due to their wide ranging applications in biomedicine, especially in cancer treatment [1-3]. One of the most promising methods is the magnetically targeted hyperthermia, which is based on the use of magnetic nanostructures to eliminate cancer cells, without damaging healthy ones, by applying an ac magnetic field to heat them up locally [1]. The heating efficiency of the nanostructures is given by the specific absorption rate (SAR). The future of magnetic hyperthermia relies on developing nanostructures with the highest possible SAR in order to reduce the amount of material needed. Motivated by their biocompatibility and colloidal stability, most research has focused on the use of small (< 20 nm) γ-Fe_2O_3/Fe_3O_4 superparamagnetic nanoparticles [3]. Due to their relatively small magnetic moments, however, it is challenging to obtain a sufficient rise in temperature throughout the entire volume of the tumor.

Therefore, we have developed alternative strategies to improve the heating efficiency of the existing magnetic nanomaterials, which include:

1. Synthesis and characterization of monodisperse Fe_3O_4 nanoparticles with controlled sizes and shapes (sphere, cube, and octopus) for magnetic hyperthermia
2. Synthesis and characterization of novel exchange-coupled FeO/Fe_3O_4 nanoparticles with tunable magnetic properties for magnetic hyperthermia
3. Synthesis and characterization of novel FeCo nanowires with enhanced heating powers and controllable dimensions for magnetic hyperthermia

In the following sections, we will discuss the motivations and highlight the new findings of each strategy.

1. Iron oxide nanoparticles with controlled morphology for magnetic hyperthermia

Iron oxide nanoparticles with a spherical shape have been extensively investigated for applications in magnetic hyperthermia due to their biocompatibility and colloidal stability. However, these nanoparticles possess low saturation magnetization and anisotropy, thus reducing their heating efficiency [3]. In this work we have developed an alternative approach to enhancing magnetic anisotropy and improving the heating capacity of a nanomaterial by modifying its shape.

Spherical, cubic, and octopod iron oxide nanoparticles with varying sizes of 15-20 nm were successfully synthesized, and their heating rates in different ac magnetic fields were systematically investigated. The nanoparticles were synthesized by a standard thermal decomposition technique as described in detail in our earlier reports and publications [4,5]. An EasyHeat LI 4.2 kW (Ambrell) based heating system that operates over a wide frequency range of 140 to 400 kHz has been used for hyperthermia tests. This system is composed of an ac field generator, a water-cooled induction coil of Cu, and a fiber optic temperature sensor.

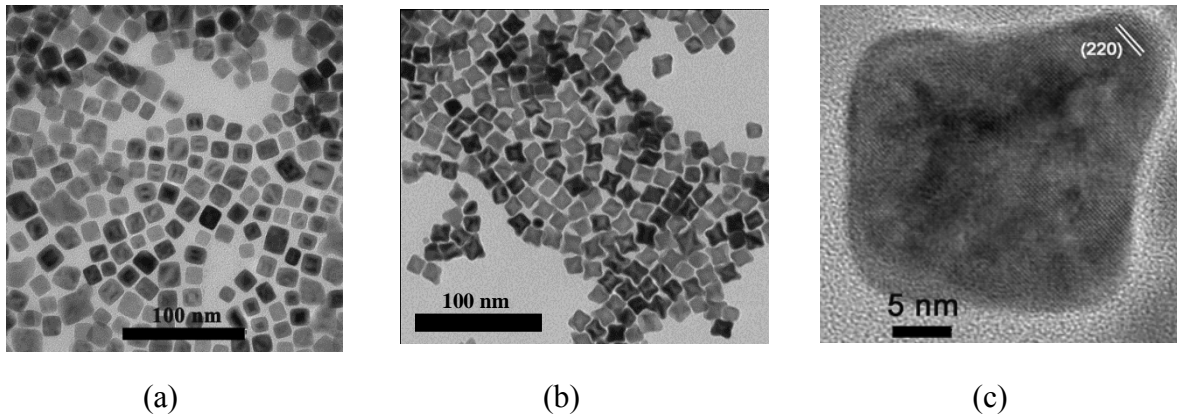(a)   (b)   (c)

Figure 1: TEM images of (a) cubic and (b) octopod nanoparticles, and (c) HRTEM image of an octopod-shaped nanoparticle.

Figure 1 shows TEM images of (a) cubic and (b) octopod iron oxide nanoparticles with the same size (~20 nm), and (c) an HR-TEM image of an iron oxide octopod-shaped nanoparticle. The good quality of these nanostructures has allowed us to analyze and understand the effect of morphology on the heating efficiency. Herein, the heat generation capacity of nanoparticles is given by the specific absorption rate (SAR), which can be defined as [1]

$$SAR = \left(\frac{m_s}{m_n}\right) C_p \left(\frac{dT}{dt}\right), \qquad (1)$$

where m_s is the mass of the solution, m_n is the mass of nanoparticles, C_p is the heat capacity of the dispersion, and dT/dt is the slope of a heating curve. The SAR value can also be associated with hysteresis losses, being given by the product of the area of the hysteresis loop and the frequency of the applied magnetic field, $SAR = A \times f$. Therefore, by increasing the anisotropy and/or the saturation magnetization, SAR values will be increased. All the measurements were carried by applying an ac field (310 kHz) for 5 minutes to each sample and measuring the temperature rise with a fiber optic temperature sensor directly inserted into the particle solution

(water or agar). For both the nanoparticles and nanowires, the same concentration of 0.5 mg/ml was employed during these experiments.

Figure 2 shows the magnetic heating curves of iron oxide nanoparticles with similar sizes (15-20 nm) but three different morphologies (sphere, cube, and octopod). It can be seen that with increasing asymmetry and surface modification of the nanoparticles, the heating efficiency progressively improves. As indicated in Figure 2(c), the SAR values obtained at 300 Oe for the octopods (150 W/g) are nearly three times larger than those for the spheres (60 W/g), and this difference increases with increasing applied magnetic field. These results demonstrate that by changing the morphology of iron oxide nanoparticles, which only requires minor adjustments during synthesis processes, we can greatly improve the magnetic hyperthermia response of the nanoparticles. This enhancement is attributed to the increase in effective anisotropy field of the nanoparticles, as the change in their morphology resulted in the bigger area of the hysteresis loop, and therefore the higher SAR values.
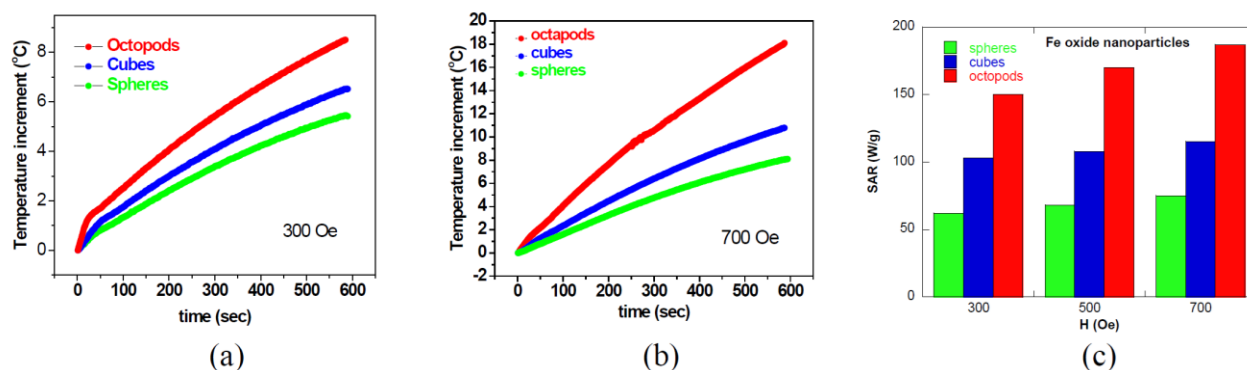

(a) (b) (c)

Figure 2: Heating curves measured at (a) 350 and (b) 700 Oe, and corresponding (c) SAR values obtained for spherical, cubic and octopod iron oxide nanoparticles.

Since the octopod-shaped nanoparticles are found to show the highest SAR, we have attempted to tune the size of these nanoparticles from 20 nm from 40 nm, and investigated their hyperthermia responses in different ac magnetic fields. The high surface to volume ratio is a unique aspect of this morphology than their spherical and cubic counterparts [5]. The nanoparticles were synthesized by a standard thermal decomposition technique as described above. The temperature dependence of magnetization was measured in the zero-filed-cooled (ZFC) and field-cooled (FC) regimes with an applied dc field of 50 Oe. The blocking temperature is above 350 K due to the large size of the nanoparticles. The high irreversibility and decrease of the FC curve with decreasing temperature suggest a disordered state at low temperatures, probably due to the competition of the interactions, anisotropies, etc. By increasing the size of the octopods from 20 to 30 nm, their H_c, M_s and M_r/M_s increase. However, when going from 30 to 40 nm, there is a decrease of H_c, M_s and M_r/M_s. In order to obtain an estimation of the effective anisotropy and how it evolves with size of the nanoparticles, we have used the law of approach to saturation [6]. The law of approach to saturation describes the field dependence of magnetization in a universal form. Under a strong magnetic field, ferromagnetic materials are generally magnetized to their saturated state, where all the moments are aligned in the same direction as the applied field. The law of approach to saturation is

$$M = M_s \left(1 - \frac{A}{H} - \frac{B}{H^2} - \frac{C}{H^2} - \cdots .. \right) + \chi_o H, \qquad (2)$$

where M_s is the saturation magnetization and constants B, C depend on anisotropy and saturation magnetization. The last term H arises from an increase in spontaneous magnetization by an external field and is called the high field susceptibility, which is a function of temperature. The origin of the first term (A/H) was explained as a result of a stress field due to dislocation, non-magnetic inclusions or voids, and it is only valid within some finite field strength near Curie point. Usually this term is not included in the calculation.

Assuming in the range of very high fields, magnetization takes place only via rotation process, than the term B will be determined by the magnetocrystalline anisotropy. Under very strong fields, when the angle between vectors H and M_s can be assumed to be small over the entire sample volume, Akulov [7] derived the expression for B. The value of **B** for a material with uniaxial and cubic anisotropy is given as

$$B = \frac{4}{15}\left(1 + \frac{16}{7}R + \frac{32}{21}R^2\right)\frac{K_1^2}{M_s^2} \tag{3}$$

$$C = \frac{6}{105}\left(1 + \frac{8}{3}R + \frac{32}{11}R^2\right)\frac{K_1^3}{M_s^3} \tag{4}$$

where, $R = \frac{K_2}{K_1}$. When K_2 is much smaller than K_1, the higher order terms can be ignored. The law of approach to saturation is valid only when all magnetic moments make a small angle with the field, and this is achieved only at very high fields. In this work, high field (up to 5 T) hysteresis loops are used to calculate the anisotropy value of octopods.

$$M = M_s\left(1 - \frac{b}{H^2}\right) + XH \tag{5}$$

Table 1: The Coercivity (H_c) and magnetization at 50 kOe (M_s), and estimated value of effective anisotropy (K_{eff}) using law of approach to saturation at 300K.

Size	H_c (50 K)	H_c (300 K)	M_s (50 K)	M_s (300 K)	K_{eff} (erg/cc) 300 K	K_{eff} (erg/cc) 50 K
20 nm	245	7	64.5	60.6	1.3864e+06	1.6433e+06
30 nm	720	130	78.9	76.1	1.9073e+06	2.1640e+06
40 nm	565	61	71.1	68.9	1.7903e+06	1.9665e+06

The estimated K_{eff} values are one order of magnitude bigger than those obtained in bulk iron oxide (1e+05 erg/cc), as is typical in this type of nanoparticle. These values decrease with temperature, as expected. There are also some observed changes in the saturation that could be affecting the estimation of K_{eff}. Concerning the size, the data for the octopods indicate that K_{eff} reaches a maximum for 30 nm.
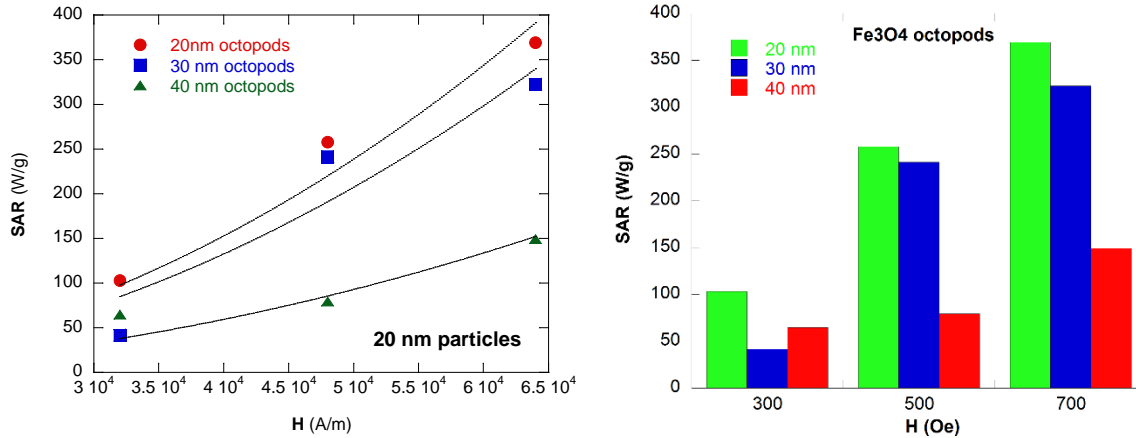
Figure 3: The SAR measured at 350, 500 and 700 Oe, and the corresponding bar graphs for 20, 30 and 40 nm octopod iron oxide nanoparticles.

As indicated in Figure 3, the SAR values obtained for 20 nm octopods at each value of field, are nearly two times larger than those for the 30 and 40 nm octopods, and this difference increases with increasing applied magnetic field. These results demonstrate that by changing the size of iron oxide nanoparticles, which only requires minor adjustments during synthesis processes, we can greatly improve the magnetic hyperthermia response of the nanoparticles. This enhancement is attributed to the increase in effective anisotropy field of the nanoparticles, as the change in their size resulted in the bigger area of the hysteresis loop, and therefore the higher SAR values.

In summary, we have successfully synthesized the iron oxide nanoparticles with controlled shapes (sphere, cube, and octopod) and found that the octopod-shaped nanoparticles possessed the largest SAR value. We have also synthesized and investigated the effects of particle size (20, 30, and 40 nm) on the heating efficiency of the iron-oxide octopod-shaped nanoparticles and have found that the 20 nm octopods possessed the highest SAR as compared to the 30 nm and 40 nm octopods. We attempt to improve the properties of these systems by increasing their colloidal stability and by comparing their results with core/shell and hollow iron-oxide nanoparticles.

2. Novel exchange-coupled FeO/Fe$_3$O$_4$ nanoparticles for magnetic hyperthermia

To address an emerging important question of how magnetic anisotropy can be manipulated to improve the heating efficiency in magnetic nanostructures, spherical and cubic exchange-coupled FeO/Fe$_3$O$_4$ nanoparticles, with different FeO:Fe$_3$O$_4$ ratios, were prepared and their magnetic and heating properties have been studied systematically. The FeO/Fe$_3$O$_4$ nanoparticles were prepared by non-hydrolytic thermal decomposition of iron-(III)acetyleacetonate (Fe-acac). The details of the synthesis procedure have been described earlier in our previous report [5]. A Bruker AXS D8 X-ray diffractometer was used to analyze the crystalline structure of the nanoparticles, and an FEI Morgagni 268 transmission electron microscope (TEM), operating at 60 kV, was used to characterize their size and shape. The magnetic properties were measured using a physical property measurement system (PPMS) by Quantum Design, with a vibrating sample magnetometer (VSM) option and a home-made transverse susceptibility (TS) options. Zero-field-cooled /field-cooled (ZFC/FC) M-T curves were measured between 10 and 350 K, with $H = 50$ Oe, while hysteresis loops, M-H, were measured at 50 and 300 K, applying fields up to $H = 50$ kOe. TS measurements were obtained at 50 and 300 K, with magnetic fields up to $H =$

20 kOe. Finally, AC magnetic hyperthermia experiments were carried out using a 4.2 kW Ambrell Easyheat LI 3542 system. The frequency was kept at 310 kHz, the amplitude of the magnetic field was tuned from 400 to 800 Oe, and during hyperthermia experiments the particles were dispersed in water and a 2% agar solution, forming a suspension of 1 mg/ml.

Figure 4 shows the XRD patterns of the FeO/Fe_3O_4 spheres and cubes. For both samples, the major peaks can be assigned to magnetite, while the small shoulders at ~36° and at 42° correspond to the FeO phase, as indentified by a graphical X-ray line profile fitting program (XFIT). The FeO peaks are more pronounced for the cubes than for the spheres. In the insets to Figure 4, TEM images of (a) spherical and (b) cubic nanoparticles are presented. It can be seen that in contrast to the spheres, the cubes tend to self-assemble forming chains and similar structures, which modify the effective anisotropy of the system.
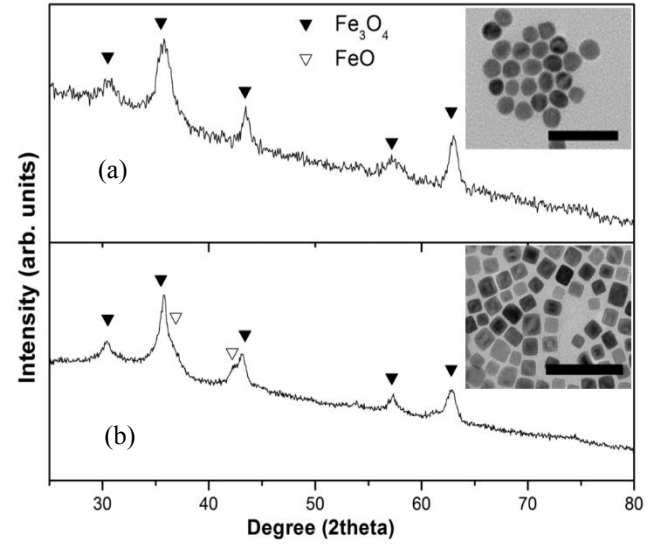
Figure 4: XRD data for the spheres (a) and cubes (b), used in this study. The open symbols represent FeO peaks and closed symbol represent Fe_3O_4 standard reflections. In the insets, TEM image of cubic and spherical particles are presented.
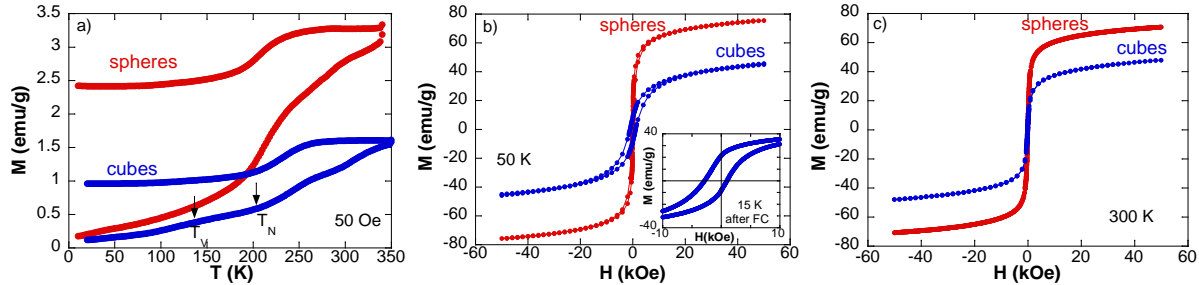

Figure 5: a) ZFC-FC curves of the spheres and cubes measured at 50 Oe. Hysteresis loops measured at b) 50 and c) 300 K for both samples. In the inset to b), the shifted hysteresis loop of the cubes after FC at 50 kOe is presented.

In Figure 5(a), we compare the ZFC/FC M-T curves measured at 50 Oe for the spheres and cubes. As can be observed, the magnetic behavior for both samples is very similar and resembles those reported earlier in similar FeO/Fe_3O_4 systems [5]. The magnetization increases with increasing temperature in the investigated temperature range, and the maximum in the ZFC M-T curve appears to be at $T > 350$ K, indicating that the nanoparticles are in a magnetically blocked state in all our measurements. The ZFC M-T curves present some distinctive features, marked by changes in the derivative, as indicated in the figure. The change of slope around $T_N \sim 200$ K can be attributed to the Neel transition of FeO, while a small bump observed at $T_V \sim 140$ K in the ZFC M-T curve for the cubes has been linked to the Verwey transition of Fe_3O_4. The FC M-T curve remains practically constant below T_N, suggesting the presence of a collective spin/glass like state at low temperatures [8].

Table 2: Magnetization, coercivity and normalized remanence at 300 K and 50 K, for cubes and spheres.

	Hc (50 K)	Hc (300 K)	Ms (50 K)	Ms (300 K)	Mr/Ms (50 K)	Mr/Ms (300 K)
Spheres	60	5	75.4	70.7	0.11	0.00
Cubes	1050	60	45.4	47.6	0.21	0.05

Figure 5(b,c) presents the hysteresis (M-H) loops for both samples at 50 and 300 K, which is below T_V and above T_N, respectively. It can be seen that the cubes have a lower saturation magnetization, M_S, but a higher coercivity, H_C, and a higher normalized remanence Mr/M_S, as compared to the spheres (see Table 2). For the spheres, M_S is around 70-75 emu/g, while for the cubes it remains around 45-47 emu/g. As compared to the spheres, the smaller value of M_S for the cubes is consistent with the fact that this sample has a higher FeO/Fe_3O_4 proportion (as revealed by the above XRD analysis), where $M_S = 80$-100 emu/g for Fe_3O_4 nanoparticles and $M_S < 20$ emu/g for FeO nanoparticles. The higher amount of FeO also explains the larger H_C value for the cubes, especially at low temperatures, since an increase in the FeO/Fe_3O_4 interface area yields a higher anisotropic effect and therefore a larger coercivity. This is also corroborated by a horizontal shift in the field-cooled M-H loop (the so-called exchange bias effect, $H_{EB} \sim 950$ Oe) observed for the cubes after cooling the sample down to 15 K in the presence of a field of 50 kOe (see the inset to Figure 5(b)). As we noted above, the cubic nanoparticles formed linear arrangements, thus giving rise to the enhanced anisotropy.
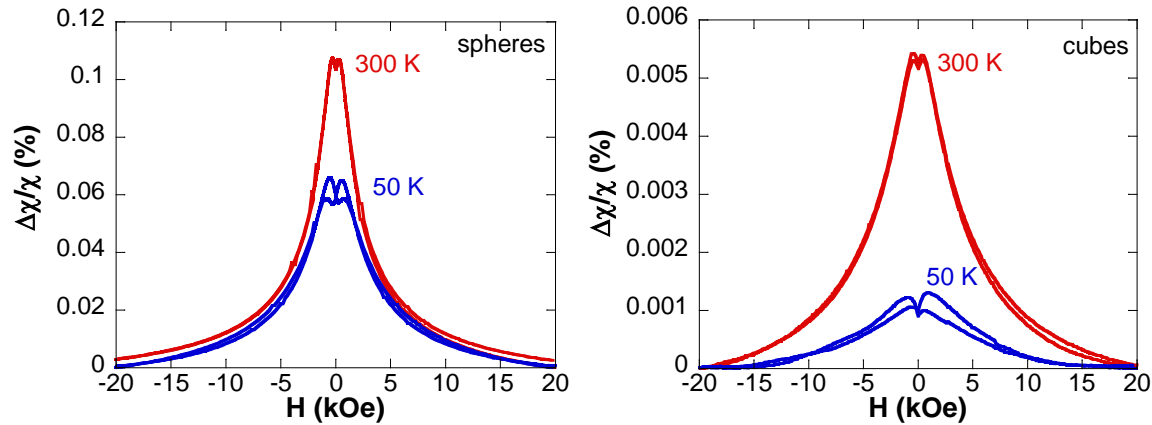

Figure 6: Transverse susceptibility measurements for a) nanospheres and b) nanocubes at 50 and 300 K.

To quantify the effects of effective anisotropy on the magnetic hyperthermia response, we have used a precise, self-resonant tunnel-diode oscillator based transversal susceptibility (TS) technique, which has been proven by us over the years as a direct probe of effective anisotropy fields in a wide range of magnetic materials [9,10]. Details of the technique and related theoretical models have been reported and discussed in our previous work [9]. The sample is housed in an inductive RF coil, which generates a small amplitude (< 5 Oe) ac field H_{ac} to perturb the magnetization of the sample. The change resonant frequency of the circuit under the influence of a changing external dc magnetic field H can be directly related to the sample susceptibility through the inductance. The relative change in transverse susceptibility is expressed by

$$\frac{\Delta\chi_T}{\chi_T}(\%) = \frac{\chi_T(H_{max}) - \chi_T(H)}{\chi_T(H_{max})} \times 100,$$

where H_{max} is the maximum applied dc magnetic field. Figure 6 shows the bipolar TS scans taken at 300 K and 50 K, where the magnetic field is swept first from positive to negative saturation and vice versa. As can be seen, the TS curves present two peaks, corresponding to the effective anisotropy fields ($\pm H_K$), and are quite broadened because of the distribution in particle size and anisotropy fields. At 300 K both TS scans are practically symmetric, and the peak positions (H_K) are determined to be ~295 and ~425 Oe for the spheres and the cubes, respectively. The larger value of H_K for the cubes as compared to the spheres is consistent with the M-H data. At 50 K, the peaks are no longer symmetric and there is a clear difference in peak height. A similar behavior has been observed in Co/CoO exchange-coupled nanoparticles [10], which has been related to the freezing of the magnetic moments of the antiferromagnetic material below T_N, thus inducing an additional anisotropy in the system. Therefore, the H_K for both samples increases at lower temperatures; at 50 K H_K = 925 and 745 Oe for the cubes and spheres, respectively. It can also be observed that the peak height ($\Delta\chi/\chi_{max}$) of the TS curves is much higher for the spheres than for the cubes. This can be associated with the larger amount of FeO inside the cubes, consistent with the above M-H data and analysis. At room temperature, close to the temperature range desirable for hyperthermia therapy (30 - 50 °C), we obtain: (i) H_k is ~1.5 times larger for the cubes and (ii) M_S is ~1.6 times larger for the spheres. These are expected to have different influences on the SAR of the nanoparticles.

To verify this, we have calculated the SAR values for both samples by using the calorimetric methods. The heating curves are presented in Figure 7(a). As depicted, with increasing field the heating rate progressively increases. Therefore, by changing the field we can easily reach the desired 40-44°C range, where the cancer cells are more susceptible to heat than healthy ones.[2] It can also be seen that the heating rate is higher for the cubes than for the spheres. This becomes more obvious by comparing the SAR values in Figure 7(b). In connection with the TS data, we can infer that increasing the effective anisotropy yields a higher value of SAR in exchange-coupled FeO/Fe$_3$O$_4$ nanoparticles with reduced saturation magnetization, demonstrating the importance of magnetic anisotropy in magnetic hyperthermia.
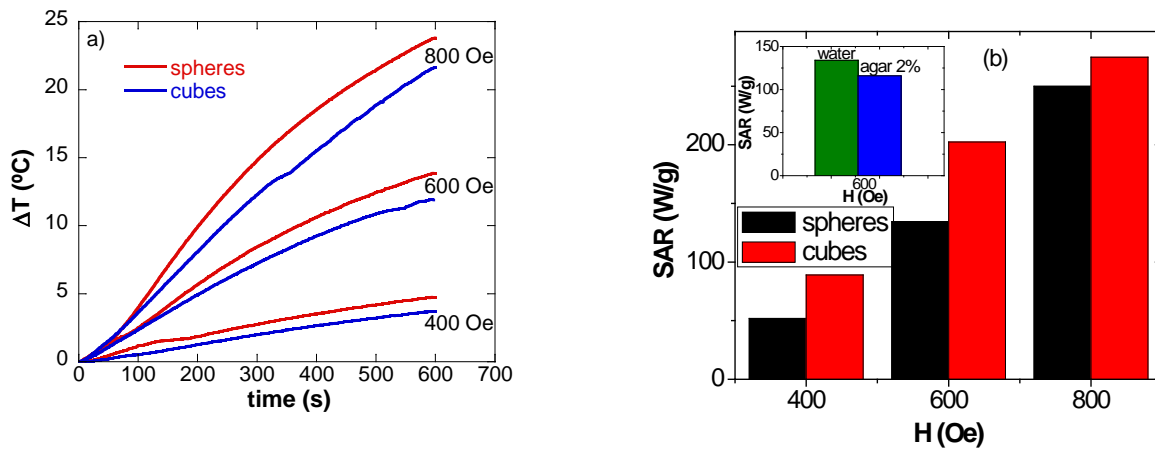

Figure 7: a) Heating curves for the spheres and cubes measured at 310 kHz and H = 400-800 Oe. b) SAR values obtained from the heating curves. In the inset, the SAR values (600 Oe) for the nanospheres in water and in agar are compared.

To better evaluate the heating efficiency of the nanoparticles, we have also embedded them in agar dispersions that are known to mimic the higher viscosity of cancer cells, while restricting the physical rotation of the nanoparticles. In the inset to Figure 7(b) we compare the SAR values obtained for the spheres, when they are in water (green column), and in agar (blue column). As observed, the SAR value decreases a bit (less than 10%) when the spheres are dispersed in agar, indicating a small contribution from the physical rotation of the nanoparticles to the heating efficiency. A similar result has also been obtained for the cubes.

In summary, we have successfully synthesized two systems of 20 nm FeO/Fe_3O_4 nanoparticles with spherical and cubic shapes. By controlling the FeO/Fe_3O_4 ratio and nanoparticle morphology, we were able to tune their magnetization saturation and effective anisotropy and consequently the heating efficiency. As compared to the spheres, the cubes possess a smaller M_S but a larger H_k and a larger SAR. This finding pinpoints the possibility of improving SAR in exchange-coupled magnetic nanoparticle systems by tuning their effective anisotropy, which is more desirable from a materials engineering perspective. The main findings of this work have been submitted for publication in *Journal of Applied Physics*, 2014.

3. Novel FeCo nanowires with enhanced heating powers for magnetic hyperthermia

Theoretical studies have predicted that the use of Fe or FeCo nanoparticles with larger magnetic moments and larger magnetic anisotropy would be more desirable than iron oxide nanoparticles, as the larger values of SAR can be achieved at smaller particle sizes [11,12]. While the magnetic anisotropy of such nanoparticles can be enhanced by considering shape anisotropy, only a few studies have taken into account the possibility of changing their aspect ratio (shape anisotropy) and, hence, tuning their effective anisotropy. Recently, Martínez-Boubeta et al. have experimentally demonstrated that highly anisotropic long chains of nanoparticles give rise to a notable increase of the SAR [13]. Taking this into account, chain-like magnetic nanostructures, such as magnetic nanowires, represent a very promising candidate for enhanced magnetic hyperthermia. Of particular interest, FeCo-based nanowires with high magnetic moments per volume can provide large forces and torques. They can also be electrodeposited in variable size templates ranging from nanometer to micrometer dimensions, thus spanning many relevant biological length scales, and their diameter and length can be independently tuned. Despite these previous studies, the effects of nanowire morphology on the SAR have not been yet investigated in detail.

Therefore, we have performed a systematic study of the effect of varying lengths (2-40 μm) and diameters (100 and 300 nm) on the magnetic and SAR responses of electrodeposited FeCo nanowires. Our study shows that these nanowires are a promising candidate for enhanced magnetic hyperthermia. Here, $Fe_{55}Co_{45}$ nanowires with different lengths (2-40 μm) and diameters (100 and 300 nm) were prepared by electrochemical deposition of Fe and Co in anodized alumina templates. We used commercially prepared AAO templates which had pore diameters of 100 nm (300 nm), an average center to center spacing of ~300 nm (700 nm) between the pores and a template thickness of 50 μm. Before electrodeposition, a 100 nm layer of Cu was sputtered on one side of the template to work as an electrode. The electrolyte consisted of salts of 0.1 m solutions of $CoCl_2.6H_2O$ and $FeCl_2.xH_2O$ each. The electrodeposition was carried out for 50 minutes at room temperature using a dc voltage at an initial current density of 100 A/m^2 via a graphite electrode. A variation of current density indicates the

deposition of Fe and Co within the AAO template. Diluted NaOH and H_2SO_4 were used to adjust the pH of the solution at the desired values. The length of the nanowires can be easily controlled by varying the deposition time. For structural characterization and hyperthermia experiments, the as-deposited nanowires were removed from the template by dissolving the template in a 1M NaOH solution.

Figure 8a shows the XRD micrographs of a typical sample of nanowires after etching out the template. All diffraction peaks correspond to the body-centered-cubic (bcc) FeCo phase. The calculation of crystalline size using Scherrer's formula indicates that these wires are polycrystalline with an average grain size of ~10 nm. A cross-sectional SEM image of an AAO template with arrays of nanowires is shown in Figure 8b. EDS analysis indicated that all samples had 55:45 % Fe:Co atomic ratios. The TEM images of the nanowires (Figure 8c) indicate that more than 80% of nanowires retained their original length after dissolving the template.
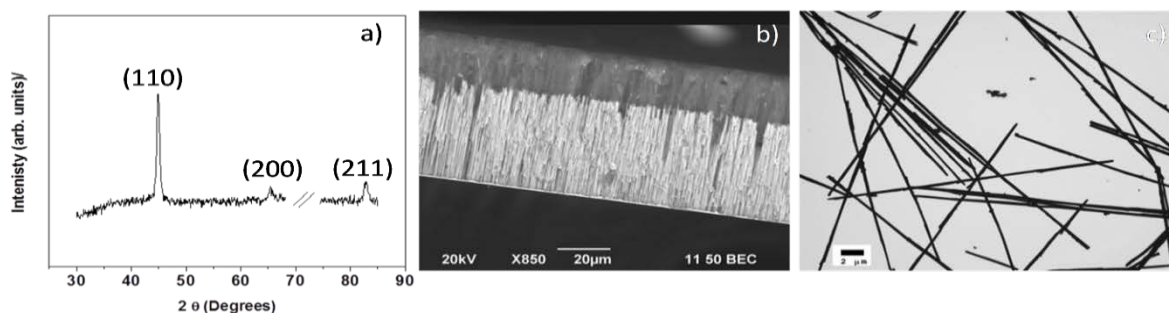

Figure 8: (a) Powder X- ray diffraction of the template-free FeCo nanowires on Si substrate. The (111) crystalline peak from Si wafer has been omitted by inserting a break in the 2 theta angle axis; (b) an SEM cross-sectional view of the FeCo nanowires embedded in the AAO template; and (c) a TEM image of the FeCo nanowires on a Cu grid.

Magnetic hysteresis measurements on the nanowires have revealed that dipolar interactions play an important role in determining the shape of the hysteresis loops and are, therefore, expected to contribute to the heating efficiency of the nanowires. To confirm this, we have studied the magnetic hyperthermia response of these nanowires. We observed that during hyperthermia experiments in water, the nanowires formed self-assembled arrays in the direction of applied fields above 200 Oe, which could be attributed to the effect of dipolar interactions. We present the heating curves for the nanowires in Figure 9a as a function of their length and diameter. With decreasing length and/or diameter of the nanowires, the heating rate decreases, but even for the smallest studied nanowires, 2 μm, their heating rate is still noticeable. As can be seen in the inset of Figure 9a, the obtained SAR values, at 300 Oe and 310 kHz, rapidly increase from 350 to 1500 W/g-$_{Fe3O4}$ when the length increases from 2 to 10 μm, and then the SAR increase slows down, reaching a maximum value of 1510 W/g for the 40 μm sample. On the other hand, the SAR values decrease by 20% when the diameter is reduced from 300 to 100 nm, but they seem to follow a similar trend. The large values of SAR of the FeCo nanowires result mainly from their large saturation magnetization combined with their shape anisotropy and the effect of dipolar interactions between the FeCo nanowires. The dependence of SAR on wire length is mainly of magnetostatic origin (shape anisotropy). The saturation trend of SAR with wire length

(inset of Figure 9a) might be correlated with the wire demagnetization factor's dependence on length and with the length at which two domains may appear along the length.
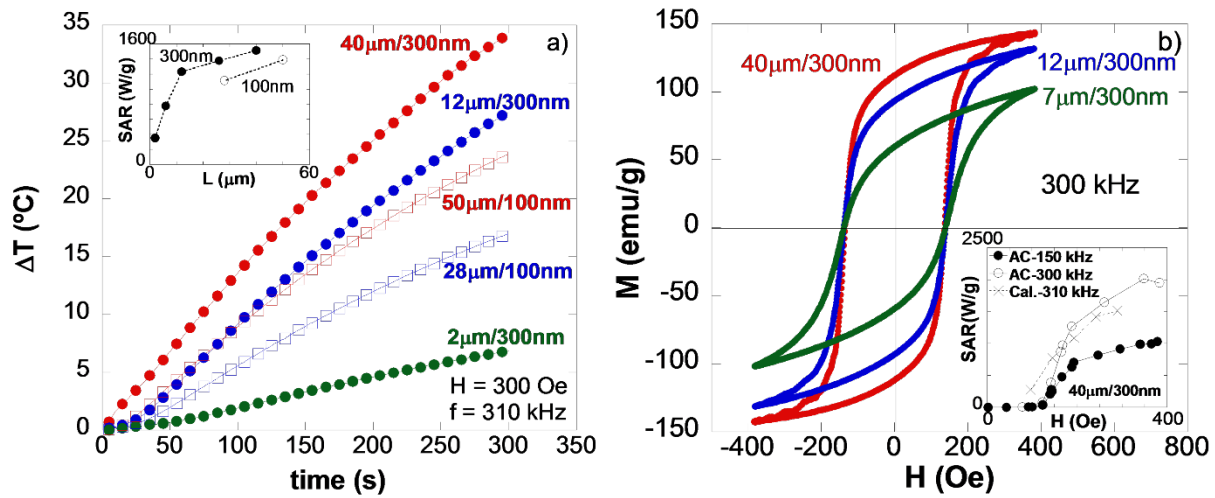

Figure 9: M-H curves as a function of (a) the length and (b) the diameter of the FeCo nanowires inside the AAO templates and aligned parallel to the magnetic field. The inset of (a) shows the coercivity as a function of the length, while the inset of Fig. (b) shows the M-H loops measured in the parallel and perpendicular directions of the applied field.

To further probe the effect of wire alignment on the heating efficiency, we have embedded the nanowires in a $2\%_{weight}$ agar solution. This method enabled us to restrict the physical movement of the nanowires while simulating the viscosity of cancer cells. Figure 10 displays the SAR values obtained for the 40 and 2 μm nanowires with different configurations. As observed, for the largest nanowires, the SAR value slightly decreased (by 7%) as the nanowires were aligned with the magnetic field in agar, whereas a drastic reduction in SAR (by 40%) was observed as the nanowires were randomly oriented. This indicates that (i) the SAR is maximized when the nanowires are aligned in the direction of the field, and (ii) the physical movement contribution of the nanowires to the SAR is relatively small. On the other hand, reducing the size of the nanowires was found to result in a greater decrease in SAR (by 25%) for the aligned nanowires. This can be associated with a better alignment of the larger nanowires, as well as their stronger dipolar inter-wire interactions.
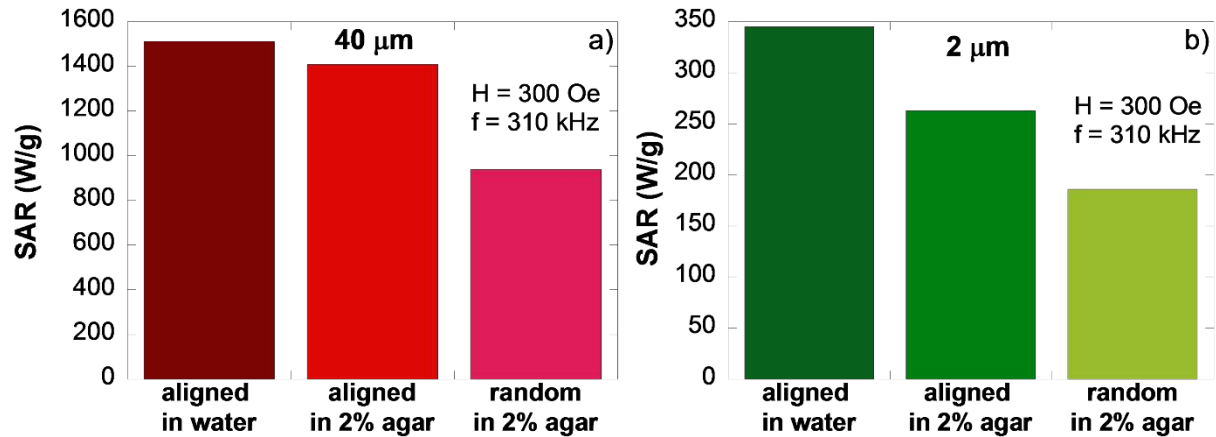
Figure 10: SAR values for (a) the 40 μm and (b) 2 μm FeCo nanowires, when dispersed in water, or in a 2% weight agar solution with different orientations.

In summary, we have performed a comparative study of the magnetic hyperthermia properties of FeCo nanowires with different lengths and diameters. We find that when the applied field is higher than the coercive field of the nanowires, the nanowires are aligned in the direction of the magnetic field during hyperthermia experiments, due to their aspect ratio and dipolar interactions. This gives rise to an enhanced heating efficiency. Magnetic hysteresis losses dominantly contribute to the heating efficiency. The SAR of the nanowires increases with an increase in the wire length (especially above 10 μm), but even for the smallest nanowires (2 μm) the obtained SAR values (up to 350 W/g, at $H = 300$ Oe and $f = 310$ kHz) are remarkable, indicating that the FeCo nanowires are a promising candidate for enhanced magnetic hyperthermia. The main results of this study have been accepted for publication in *Journal of Applied Physics*, 2014.

B. High aspect-ratio magnetic nanostructures for novel biosensors and microwave device applications

There is an increasing need for the use of nanostructured materials with tunable and anisotropic magnetic properties. However, the ability to tune the magnetic anisotropy of magnetic nanoparticles to meet the needs of vastly different applications is a challenge. Recently we have introduced a new concept of incorporating superparamagnetic nanoparticles such as magnetite (Fe_3O_4) and cobalt ferrite ($CoFe_2O_4$) into a polymer matrix to create a new class of nanocomposite materials with tunable microwave response [14,15]. We propose that the microwave response can be further enhanced in high-aspect ratio magnetic nanostructures, such as carbon nanotubes (CNTs) filled with supermagnetic nanoparticles, where the magnetic anisotropy can easily be tuned by varying the size and density of magnetic nanoparticles inside CNTs. Previously, we have reported the synthesis and characterization of CNTs filled with magnetite, cobalt ferrite and nickel ferrite nanoparticles [16]. Interestingly, all ferrite-filled CNTs show enhanced interparticle interactions relative to the nanoparticles alone. Our results revealed the new possibility of tuning the magnetic properties of nanoparticle-filled CNTs for sensor and microwave device applications. In this project, we have successfully filled CNTs with

1. with superparamagnetic NiFeO nanoparticles
2. with core/shell structured Fe/γFe$_2$O$_3$ nanoparticles with anisotropic magnetic properties

17

In addition, we have developed a novel magnetic nanostructure composed of polymer thin films with Fe_3O_4 nanoparticle-filled nanoholes arrays. In the following sections, we will emphasize the main results of these studies.

1. Superparamagnetic properties of carbon nanotubes filled with NiFe₂O₄ nanoparticles

One-dimensional magnetic nanostructures composed of multiwalled carbon nanotubes (MWCNTs) filled with magnetic nanoparticles are very promising for a variety of applications ranging from electromagnetic interference shielding to water purification, and biomedical applications such as hyperthermia and targeted drug delivery [17-19]. The fabrication of uniform MWCNTs with reduced diameters (below 100 nm) is presently a challenging task. In our previous work, MWCNTs synthesized using commercially available templates were successfully filled with magnetite nanoparticles (Fe_3O_4) [16]. During that study, however, we found that commercial alumina templates used in MWCNT growth generally yield non-uniform magnetic properties due to poor uniformity in pore size throughout the template thickness. Synthesis of customized templates with better pore diameter control is essential to overcome these limitations.
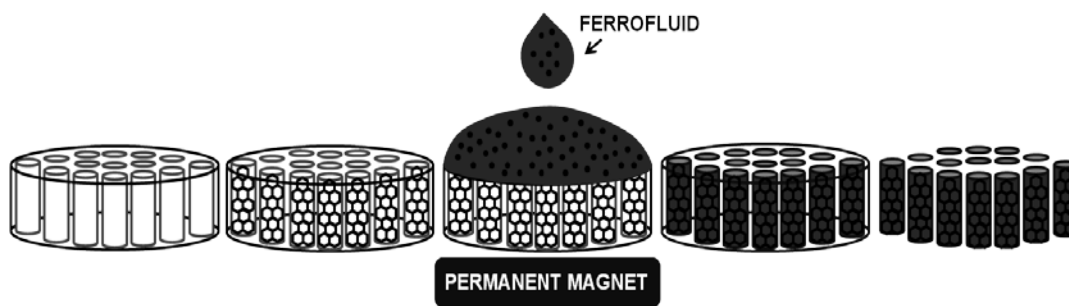
Scheme 1: A schematic of the CNTs filling process with C/S NPs.

We present results from MWCNTs successfully synthesized using custom-made 80 nm pore-size alumina templates, filled with nickel ferrite (NFO) nanoparticles of 7.4 ± 1.7 nm in diameter. Detailed magnetic characterization was performed using DC and AC susceptibility experiments. $NiFe_2O_4$ nanoparticles were synthesized in-house using a thermal decomposition method. The final product was suspended in high-purity hexane to create a ferrofluid. Custom highly ordered anodic aluminum oxide (AAO) membranes were fabricated from high purity aluminum foil (99.999%) by electrochemical route using a controlled two-step anodization process. In this process, electrodes were placed on both sides of a degreased and electropolished high-purity aluminum foil in a 0.3 M oxalic solution at a voltage of 40 V and 4 ºC. This first anodization formed initial seeds for the membrane pores. The alumina obtained during the first step was chemically removed using a mixture solution of CrO_3 and H_3PO_4. The resulting surface was anodized again to obtain alumina templates with hexagonally ordered self-assembled nanopores. The remaining aluminum substrate was removed by a mixed solution of $CuCl_2 \cdot 2H_2O$ and HCl. In order to obtain pores with openings at both sides, the alumina barrier layer was chemically etched by an H_3PO_4 solution. These membranes were later used as templates for MWCNT synthesis and filling. MWCNTs were synthesized using a catalyst-free method via chemical vapor deposition. Prior to MWCNT growth, an alumina template was heat-treated at 640° C to avoid warping during synthesis. The heat-treated template was then placed at the heat source and heated to 620° C under the flow of argon gas. Once at the reaction temperature, helium and ethylene gas were introduced at flow rates of 70 and 30 sccm, respectively, and the

flow of argon gas was terminated. This ratio was maintained for 5.5 hours, before the MWCNT-filled alumina template was allowed to cool (see Scheme 1).
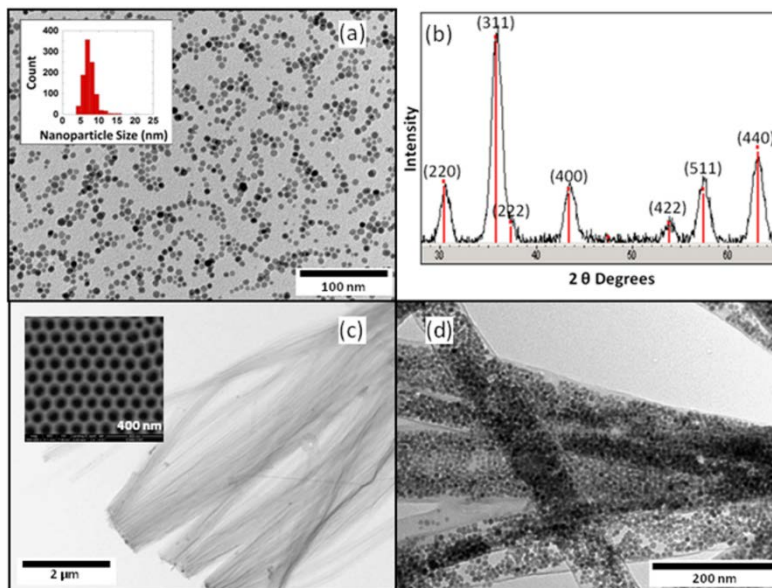

Figure 11: TEM image of nickel ferrite nanoparticles with histogram inset showing particle size distribution (a); XRD plot showing peaks for inverse spinel structure of nickel ferrite nanoparticles (b); TEM image of free-standing MWCNTs with inset showing SEM of hexagonally-ordered pores in the alumina membrane (c); TEM image of nickel-ferrite-filled MWCNTs (d).

Following synthesis, MWCNTs were filled with nanoparticles. The alumina template containing MWCNTs was filled with nanoparticles using a magnetically-assisted capillary action [16]. The MWCNT-rich alumina template was placed atop a permanent magnet ($\mu_0 H = 0.5$ T), and the previously synthesized ferrofluid was slowly dropped on to the surface of the alumina template so that the nanoparticles were able to coat the inner walls of the MWCNTs. Finally, the alumina template was dissolved by gently crushing the nanoparticle-filled alumina template and sonicating in an 8 molar solution of sodium hydroxide and vacuum filtering through a polyester nucleopore membrane (pore size, ~200 nm). After filtration, the resulting nanoparticle-filled-MWCNTs were collected and stored in isopropanol for further structural and magnetic characterization by TEM and PPMS.

In Figure 11(a) we present the TEM image of the as-synthesized NFO nanoparticles. As observed, all of the nanoparticles exhibit spherical shape and a relatively narrow size distribution with an average size of 7.4 ± 1.7 nm, as inferred from the histogram in the inset. It can also be seen that the surfactants were employed effectively, avoiding nanoparticle agglomeration. The XRD plot obtained for the NFO nanoparticles exhibits clear diffraction peaks (Figure 11(b)) indicating that we obtained highly crystalline nanoparticles, despite their small size; they have been successfully indexed with the inverse spinel structure (AB_2O_4) characteristic of the $NiFe_2O_4$ phase. An SEM image of one of the custom-made AAO membranes is presented in the inset to Figure 11(c). It is clear to see that the AAO membranes present a well-defined and homogeneous hexagonal array of pores, with an average diameter of 80 nm and inter-pore distance of 105 nm; membrane thickness is 40 μm. Un-filled MWCNTs prepared using these membranes are imaged

in Figure 11(c). They present an outer diameter of approximately 80 nm and lengths of up to 11 μm. Finally, in Figure 11(d) we present an image of the NFO-filled MWCNTs. It is observed that no nanoparticles remain outside of the MWCNTs, and that the nanoparticle packing within the MWCNTs is quite uniform. Our past studies have revealed that whenever there is a high degree of non-uniformity and agglomeration of particles into random clusters, the magnetic properties are often irreproducible from batch to batch so this uniform packing is crucial for reproducible magnetic response needed for applications.
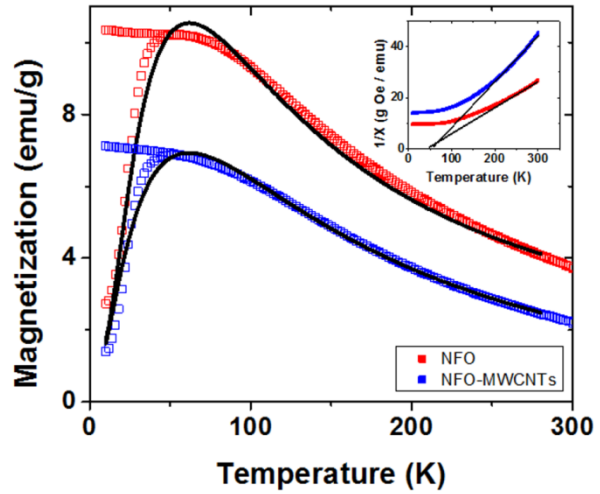

Figure 12: M-T curves using the zero-field cooled and field-cooled protocols (H=100 Oe) along with fittings of the ZFC curves; inset shows Curie-Weiss fitting using ZFC curves.

In Figure 12 we present zero-field-cooled/field-cooled (ZFC-FC) curves normalized by the mass of the samples for the NFO nanoparticles and the NFO-filled MWCNTs (NFO-CNTs). As can be seen, the curves for NFO and NFO-CNTs share a similar shape with ZFC curves presenting a defined maximum around T_B ~52 K associated with the blocking process of the nanoparticles. The irreversibility temperature (T_{irr}), where the ZFC and FC curves separate, occurs nearly at T_B, indicating monodispersity of the nanoparticles, as confirmed by TEM. No shoulder or additional maximum at very low temperatures is observed, as has been reported in similar NFO nanoparticle systems and ascribed to surface spin freezing and glassy behavior [10]. This indicates that the surface spin disorder in our nanoparticles is negligible. To probe superparamagnetic properties of our sample, we have fit the ZFC M-T curves using an appropriate expression based on the Stoner-Wohlfarth model:

$$M_{ZFC} = \int_0^{V_c} M_{ZFC}^{SPM} f(V)dV + \int_{V_C}^{\infty} M_{ZFC}^{bl} f(V)dV \qquad (6)$$

where V is the volume of the nanoparticles, $f(V)$ is the size distribution of the nanoparticles, which we have assumed to be Log-Normal; $V_c(\text{T}) = 25k_BT/K_{eff}$ is the critical volume of the nanoparticles, which marks the limit between superparamagnetic and blocked nanoparticles, K_{eff} is the effective anisotropy; finally M_{ZFC}^{SPM} and M_{ZFC}^{bl} are the magnetic contribution of the nanoparticles in a superparamagnetic and blocked state, respectively. The details of the analysis can be found in Ref. 13. In principle, this model was designed for non-interacting nanoparticles, but in a first approximation it can be considered that the presence of the interparticle interactions will mainly affect the effective anisotropy value, K. As observed, a very nice fitting is obtained in nearly the entire range of temperatures analyzed. From the fitting, we obtain an average particle size of 7.9±1.8 and 7.1±1.9 nm for the NFO and NFO-CNT samples, respectively, which are in very good agreement with TEM analysis. The effective anisotropy values are of 4.9x10^5 and 6.9x10^5 erg/cc for NFO and NFO-CNTs samples. The average particle size and effective anisotropy values for NFO-CNTs are one order of magnitude larger than the bulk magnetocrystalline anisotropy (-7 x10^4 erg/cc). As depicted in the inset of Figure 12, a good

fitting to the Curie-Weiss Law is found above 200 K with T_C close to 50 K and positive, indicating weak ferromagnetic-like interactions.
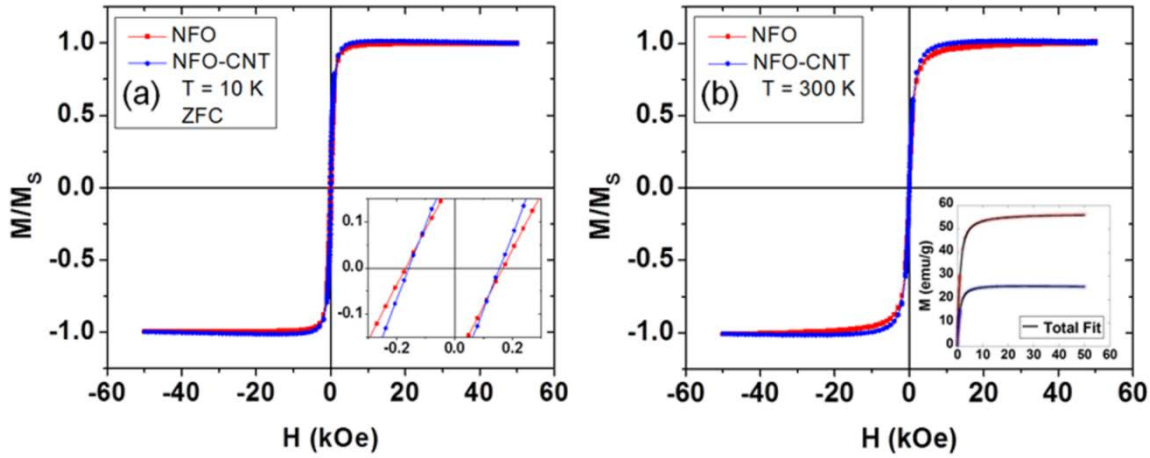

Figure 13: Magnetization vs. Magnetic Field curves at 10 K under the zero-field cooled protocol for nickel ferrite and nickel ferrite-filled MWCNTs with inset showing hysteresis (a); Magnetization vs. Magnetic Field curves at room temperature for nickel ferrite and nickel ferrite-filled MWCNTs with inset showing Langevin-function fit of each hysteresis curve (b).

Figure 13 shows M-H loops for the NFO and NFO-CNT samples at 10 K and 300 K. Note that the decrease in magnetization in the NFO-CNT sample is due to the fact that the mass includes that of the MWCNTs in addition to the NFO nanoparticles. At 10 K, the coercivity (H_C) is relatively small, 167 Oe and 155 Oe with a normalized remanence (M_R/M_S) of 0.20 and 0.22 for NFO and NFO-CNTs, respectively. No coercivity or remanence is observed in the samples at 300 K, suggesting that the 7.4 nm NFO nanoparticles exhibit SPM-like behavior at room temperature. To confirm this, we fit our hysteresis loops with a standard Langevin expression:

$$M(H) = M_S \int_0^\infty L\left(\frac{\mu H}{k_B T}\right) f(D) dD, \tag{7}$$

where D is the diameter of the nanoparticles, $f(D)$ corresponds with a Log-Normal size distribution, and $L(x) = \mathrm{cotanh}(x)-1/x$. As seen from the inset of Figure 13(b), the fittings for NFO and NFO-CNTs at 300 K are very good, although the apparent size obtained from the fittings is a little bit bigger than expected, 8.5-9 nm, which is likely due to the effect of dipolar interactions, which although weak, cannot be neglected.

AC susceptibility measurements were systematically performed on the samples by applying a 10 Oe AC field within a frequency range of 100 Hz to 10 kHz. The peak shift values are 0.05 and 0.07, for the NFO and NFO-CNTs, respectively, which are close to the values expected for super-spin glass systems. Figure 14 shows the real part, χ', of the AC susceptibility. Since we established earlier that there are weak dipolar interactions, we fit results from both samples to the Vogel-Fulcher model:

$$\tau = \tau_{VF} \exp\left(\frac{E_a}{k_B(T-T_0)}\right) \tag{8}$$

$E_a = K_{eff} V$ is defined as the anisotropy energy barrier and τ_{VF} is defined as the relaxation time of each magnetic nanoparticle. A relatively good fitting is obtained in both cases, giving values for the relaxation times around 10^{-11}-10^{-12} s; the K_{eff} values are found to be 2.2 $\times 10^5$ and 5.6×10^5 erg/cc, and $T_0 \sim 52$ and 40 K, for the NFO and NFO-CNTs, respectively. These values are slightly smaller than those obtained in the ZFC/FC fitting because in that fitting, the effect of the interactions is reflected in K_{eff}, however, here it is reflected in T_0. These results confirm a super-spin-glass-like behavior mediated by dipolar interactions for these samples at low temperatures (< 50 K). The slightly higher K_{eff} and lower T_0 for the NFO-CNTs, could be related to a slight weakening of the interactions when the nanoparticles are inside the CNTs.

In summary, we successfully synthesized 7.4 nm nickel ferrite nanoparticles encapsulated within custom multi-walled carbon nanotubes. This system exhibits superparamagnetic-like behavior with weak dipolar interactions of a ferromagnetic nature and super-spin-glass-like behavior at low temperatures. These excellent magnetic properties make these NFO-filled MWCNTs very promising for applications ranging from magnetic hyperthermia, to chemical sensing and microwave absorption.
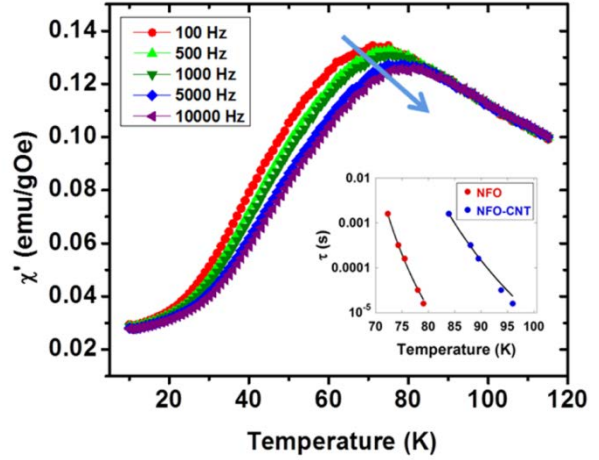

Figure 14: AC Susceptibility measurement for nickel ferrite nanoparticles used for filling with inset showing a fitting of the peaks for both the nickel ferrite and nickel ferrite-filled MWCNTs to the Vogel-Fulcher model.

2. Enhanced magnetic properties of carbon nanotubes filled with core/shell Fe/γFe₂O₃ nanoparticles:

Core/shell (C/S) structured Fe/γFe$_2$O$_3$ nanoparticles are interesting because they are hybrid nanostructures of two different materials [20]. These particles have shown very interesting magnetic behavior, such as exchange bias, super spin glass state and collective magnetic behavior, owing to their unique morphology and enhanced inter-particle and intera-particle interactions. We have successfully fabricated CNTs filled with Fe/γFe$_2$O$_3$ nanoparticles and investigated their magnetic properties. The core/shell nanoparticles were synthesized by thermally decomposing iron-pentacarbonyl using a home-build chemical synthesis setup [4].
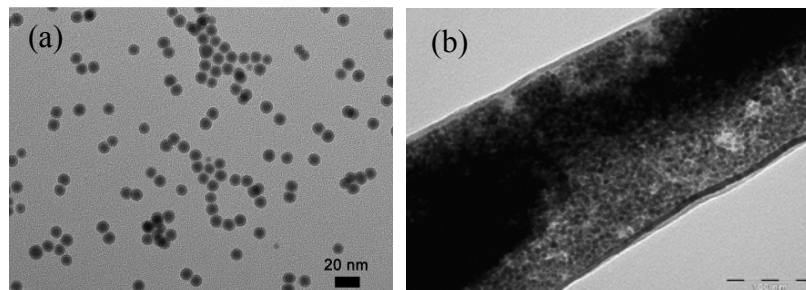

Figure 15: A TEM image of C/S Fe/γFe₂O₃ nanoparticles along with a nanoparticle-filled CNT.

Figure 15 shows the TEM image of 12.2±0.7 C/S NPs. As reported earlier, the core is made up of metallic $Fe^{(0)}$ and the shell is composed of randomly oriented grains of γFe_2O_3. With the variation of average particle size, core size varies whereas shell thickness remains same (~ 2nm). Continuing our study on nanoparticle-filled CNTs, we filled multi-walled CNTs with the core/shell $Fe/\gamma Fe_2O_3$ nanoparticles described above. The filled-CNT synthesis method is outlined in the schematic below. The CNTs were synthesized using an alumina template-assisted chemical vapor deposition growth method [16]. No catalyst was used in the synthesis of these CNTs. The alumina template, with pore size ranging from 200-350 nm, is placed vertically in the CVD furnace and gasses are flowed through it at a rate of 70 sccm for helium and 30 sccm for ethylene.
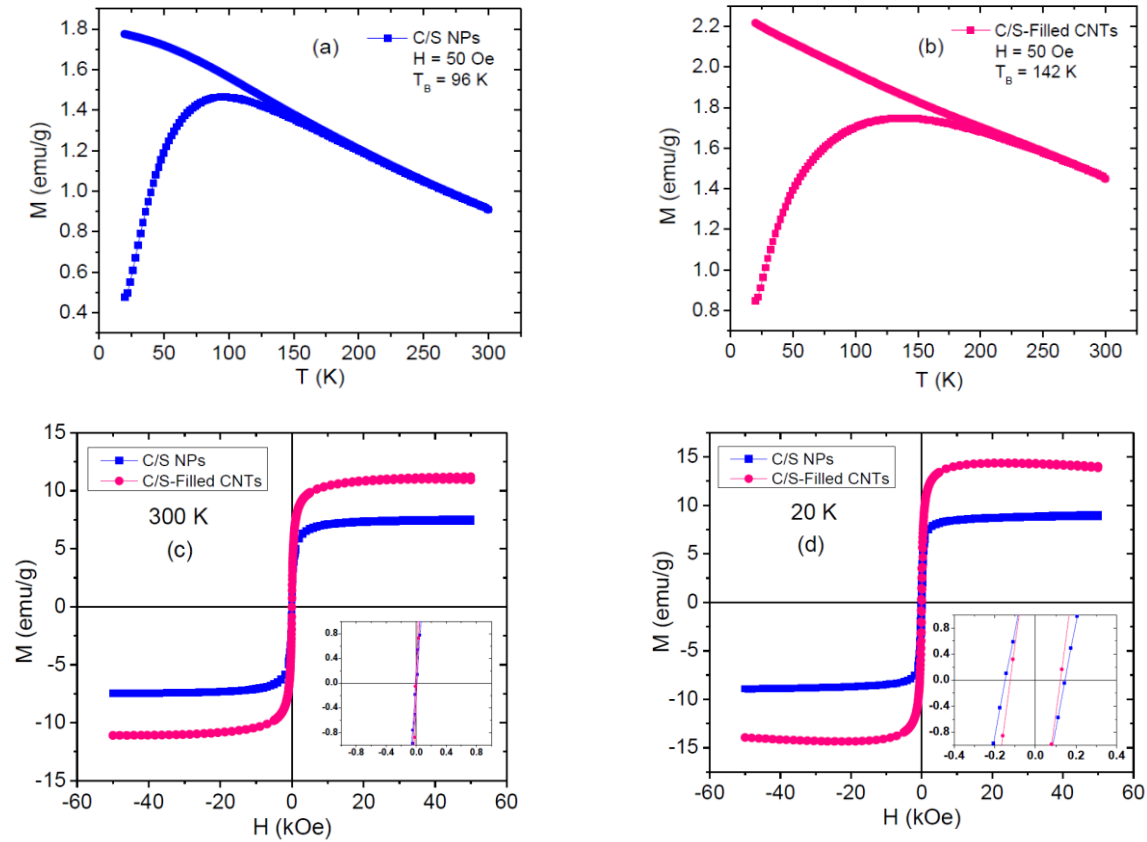

Figure 16: Temperature dependence of ZFC and FC magnetization of (a) C/S NPs and (b) C/S NPs -filled CNTs; (b,c) M-H curves taken at 300 K and 20 K for these samples.

Magnetic measurements in Figure 16 indicate that the C/S NPs have a blocking temperature of 92 K, as shown from the ZFC curve. The nanoparticles display no coercivity at room temperature, indicating a superparamagnetic nature. Coercivity at 20 K, ZFC measurement is 130 Oe. The magnetic measurements of NP-filled CNTs reveal that the blocking temperature of the C/S NPs (when encapsulated within the CNTs) increased to 145 K, which is indicative of enhanced inter-particle interactions. The M(H) measurement at 300 K, once again shows no coercivity, indicating that the nanoparticles are still in the superparamagnetic regime. From the M(H) measurement under the ZFC protocol at 20 K, the coercivity is 150 Oe. The enhanced coercivity below blocking is also indicative of enhanced inter-particle interactions. It is worth

noting that relative to C/S NPs, the saturation magnetization (M_s) is greatly enhanced in the CNTs filled with C/S NPs. This is very beneficial for the use of these novel nanostructures in biomedical applications such as hyperthermia and MRI. However, the origin of this increase in M_s remains to be investigated. Future work on this system includes taking ac susceptibility data and incorporating the filled-CNTs into polymer nanocomposites to meet the needs of vastly different applications. We are planning to systematically investigate magnetic anisotropy that plays a key role in controlling the magnetic properties in nanoparticle assemblies. In addition to the standard dc and ac magnetization measurements with the PPMS, we plan to conduct resonant radio-frequency (RF) transverse susceptibility and magneto-impedance measurements on magnetic nanoparticle-filled CNTs.

3. Highly ordered magnetite nanoparticle-filled nanohole arrays for biomedical applications

Nanoarchitecturing of thin films has emerged as a straightforward and effective way to engineer materials' properties at the nanometer level. Currently, there is an increasing need for the use of nanostructured materials with tunable and anisotropic magnetic properties. However, the ability to tune the magnetic anisotropy of magnetic nanoparticles to meet the needs of vastly different applications is a challenge [21]. Recently, the sub-100 nm nanohole arrays have been successfully fabricated from a pre-ceramic polymer mold using spin-on nanoprinting (SNAP) [22]. If these nanohole arrays can be filled with magnetic particles to create a new class of novel high-aspect ratio magnetic nanocomposites, the challenge raised above can be resolved. With this motivation, we present a simple and high throughput method to develop an array of Fe_3O_4 nanoparticle-filled nanoholes and demonstrate the unique magnetic properties of the material for a variety of applications.
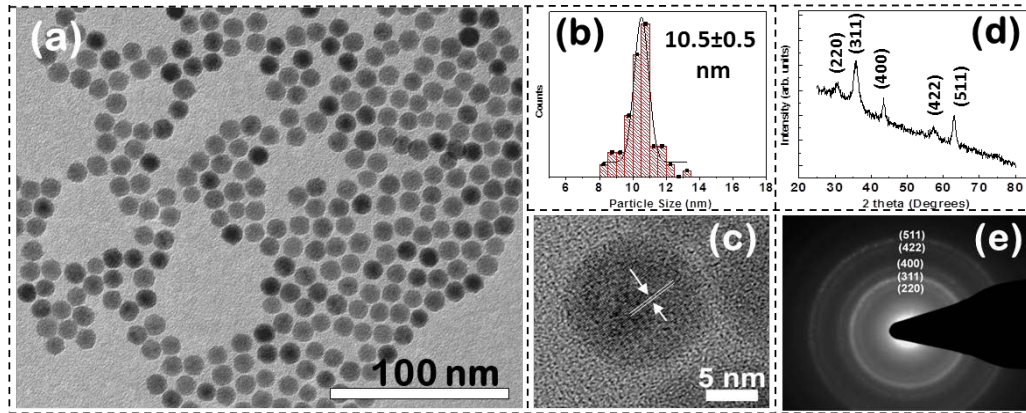

Figure 17: Bright-field TEM image of as-synthesized Fe_3O_4 nanoparticles (a), the corresponding particle size distribution (b), HRTEM image of a single Fe_3O_4 nanoparticle (c), XRD pattern (d) and SAED image of the Fe_3O_4 nanoparticles (e).

Figure 17(a) shows a bright-field TEM image of the synthesized Fe_3O_4 nanoparticles. The nanoparticles are spherical, with an average diameter of 10.5±0.5 nm determined by fitting the distribution obtained after counting more than 200 particles (Figure 17b). The HRTEM image of the nanoparticles (Figure 17c) evidences that the nanoparticles are single crystalline, as the lattice fringes continues without interruption. The calculated distance between the lattice planes in Figure 17 c is 2.1 Å, which corresponds to the (400) planes of Fe_3O_4. Figure 17d shows the

XRD pattern of the nanoparticles. All peaks are indexed to the characteristic reflections of Fe_3O_4 crystal planes. The average crystalline size, as determined from peak widths using the modified Scherrer's formula, is about 9 nm. This size is very close to that determined from the TEM, confirming the single crystalline nature of the synthesized particles. Figure 17e shows a selected area electron diffraction (SAED) image of the nanoparticles. All diffraction rings correspond to those of Fe_3O_4, which is consistent with the measured XRD pattern.

These synthesized Fe_3O_4 nanoparticles were then filled inside nanoholes patterned in a polymer film, using a novel magnetic drag and drop procedure. Figure 18a and b show SEM images of the printed nanohole arrays before and after filling with the magnetite particles. As shown in Figure 18c, uniform distribution of Fe_3O_4 nanoparticles still reside in the nanoholes after washing and removing stray particles on the patterned surface. To examine the diameter and depth of the nanoholes, we studied the SEM and AFM images obtained and the average diameter of the nanoholes observed from AFM and SEM were in good agreement. A careful data analysis of the AFM topography images indicated a distribution in diameter that is centered around 95 nm, while SEM images indicates 80 nm.
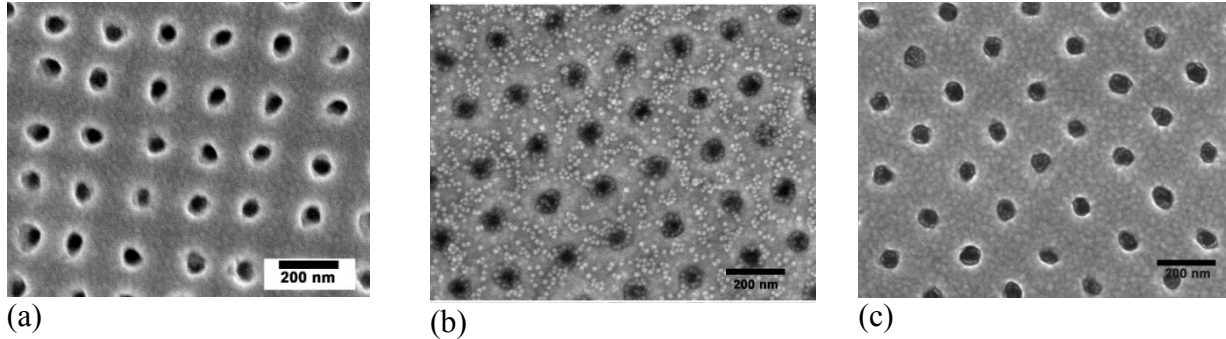

(a) (b) (c)

Figure 18: SEM images show arrays of nanoholes (a) before and (b) after filled with Fe_3O_4 nanoparticles and (c) after removing stray particles.

Magnetic measurements were performed on these magnetic nanostructures using the physical property measurement system (PPMS). We have observed that for the as-synthesized Fe_3O_4 nanoparticles, the M-H curves at 300 K do not show any hysteresis (zero coercivity, H_C, and no remnant magnetization, M_r), whereas a clear hysteresis with a coercivity of H_C ~53 mT is observed at 10 K. This is characteristic of the sample of nanoparticles being superparamagnetic at room temperature and entering a ferromagnetic (blocked) state at low temperature, which results in the opening up of the hysteresis loop. However, the case is very different for the Fe_3O_4-filled nanohole film. The M-H curve of this sample at 300 K shows a clear hysteresis, with values of H_C ~30 mT and M_r/M_S ~ 0.2. Our results suggest that other factors in addition to enhanced inter-particle interactions are also important in governing the magnetism of the Fe_3O_4-filled nanohole film.

To confirm this, MFM profiling was performed on the region of the Fe_3O_4-filled nanohole film presented in Figure 19. In our MFM measurements, the constant magnetization of the tip and its oscillation above the sample constitute a force gradient directed perpendicular to the plane of the film. The contrast seen in the MFM image (Figure 19a) can be attributed to an out-of-plane component of the magnetization, which oscillates in up and down directions to reduce

the magnetostatic energy, creating magnetic poles of alternating signs that give rise to the lower and higher phase of the tip oscillation. As one can see in this figure, the MFM pattern evidences the presence of both diametric and in-axis magnetic moments. A signal with higher intensity, shown in white here, from the diametric magnetic moment (white lobes) clearly stands out. To quantify the strength of the magnetic moments, MFM profiles (vertical/horizontal directions) across five holes in Figure 19a were collected. The sharp spike (few nm to 30nm in width) at the center of the line profiles shows the in-axis magnetic moment (Figure 19b). Note that given the small size of the sharp spike, it is difficult to create a profile crossing the spikes in each hole. MFM profiles collected from the planar region across the white lobes at the center of the square matrix are shown in Figure 19c. The strength of the in-axis and diametric magnetic moments collected from the four scan diametric lines in the center of Figure 19a is shown in Figure 19d. It is worth noting that the strength of the magnetic moments is stronger for the "vertical" case (Figure 19b) than for the "diagonal" case (Figure 19d). This can be attributed to the nanohole-nanohole interactions that appear to be stronger at shorter distances between the Fe_3O_4-filled nanoholes in the former case. These findings point to a significant impact of long-range dipolar magnetic interactions between the Fe_3O_4-filled nanoholes on the magnetism of the Fe_3O_4-filled nanohole array, and provide an important understanding of the origin of the enhanced coercivity, as well as the room temperature ferromagnetic-like behavior observed in this novel magnetic nanostructure.
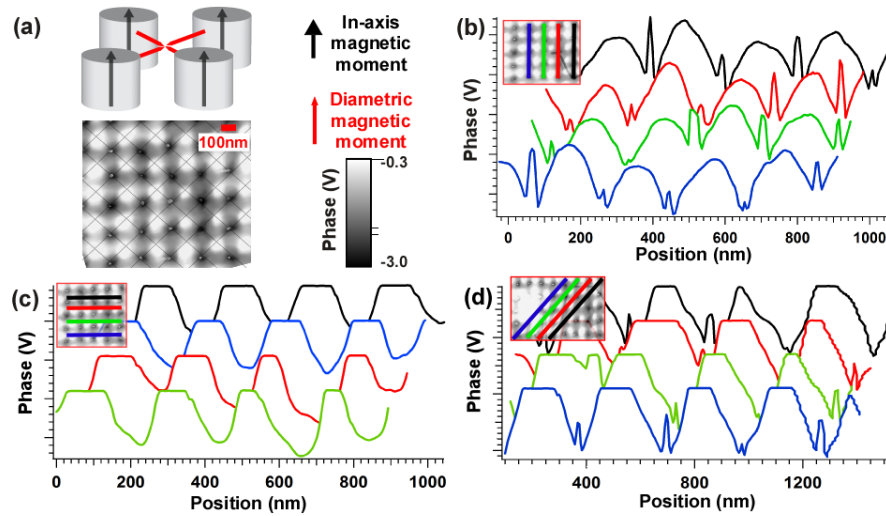

Figure 19: (a) MFM map of about 1µm×1µm area of the sample with nanoholes filled with Fe_3O_4nanoparticles. The corresponding magnetic moments of interest are depicted in the inset (top: red arrow for the diametric magnetic moment, black arrow for the in-axis magnetic moment). (b-d) Profiles extracted from the MFM image (a): (b) vertically across the nanoholes, (c) horizontally across the white lobes and (d) diagonally across the nanoholes. The locations are depicted in the respective insets (color coded black, red, green, blue).

From a magnetic devices application perspective, the enhancements in H_C and H_K achieved in the highly ordered Fe_3O_4 nanoparticle-filled nanohole arrays are desirable for their use as the magnetic media in high-density magnetic recording applications. A large enhancement of the microwave response is also expected in these highly ordered Fe_3O_4 nanoparticle-filled nanohole

arrays, the coercivity and magnetic anisotropy can easily be tuned by varying the size and density of magnetic nanoparticles inside nanoholes. This makes the present nanocomposite an attractive candidate for high-performance RF sensor and microwave device applications. Recently, the magnetic anisotropy of Fe_3O_4 nanoparticles has also been exploited to improve the detection capacity of single nanoparticles using the MFM technique [23]. In this regard, the use of a highly ordered Fe_3O_4 nanoparticle-filled nanohole array with tunable magnetic anisotropy seems more favorable for biodetection, as each Fe_3O_4 nanoparticle-filled hole can act as a sensing probe and hence detection of multiple different biomarkers/biomolecules can be achieved simultaneously using this array of patterned multi-holes.

In summary, we have developed a new type of magnetic nanostructure using the combined chemistry and SNAP techniques. This novel nanostructure can be ideally used for a wide range of applications, including their use as a biosensing probe for detection of multiple different biomarkers/biomolecules in nanobiomedicine. The main findings of the work have been reported in the journal *Small*, 2014. Our next targets will be to fill nanohole-arrayed films with functional core-shell and hollow iron-oxide nanoparticles, as well as integrating these nanostructures with the radio-frequency magnetoimpedance technology to make a novel biosensing system for applications in biodetection.

C. Soft ferromagnetic materials and magneto-impedance technology for microwave energy, chemical and biological sensing

Soft magnetic materials including Co-based amorphous microwires and ribbons are among the best candidate for sensor applications. The discovery of the so-called giant magnetoimpedance (GMI) effect in these materials makes them attractive for wide applications ranging from magnetic and stress sensing to biodetection [24]. We have tailored the GMI properties of these materials for advanced sensor and biosensing applications, which include:

1. Design and fabrication of a new class of a fiber Bragg grating-based microwave energy sensor using a soft ferromagnetic amorphous microwire
2. Design and fabrication of a novel class of soft ferromagnetic amorphous multiwire-based inductance coil sensors for advanced sensor applications
3. Development of a new type of nanoparticle-based GMI biosensor for highly sensitive detection of cancer cells and biomolecules

We present below the main results of these studies.

1. Glass-coated soft ferromagnetic amorphous microwires for microwave energy sensing

Recently, we have developed a new method of using these microwires as a microwave absorber for fabrication of a fiber Bragg grating-based microwave energy sensor with improved sensitivity and less perturbation of the microwave field [25]. As compared to a similar approach that uses gold to absorb electromagnetic radiation, the glass-coated amorphous microwire yields a device with greater sensitivity (~10 times at $f = 3.25$ GHz) relative to the perturbation of the microwave field. Nevertheless, the development of this type of sensor is still in infancy, and optimization of the overall performance in various applications requires a better understanding of the relationship between the magnetic properties, GMI, and microwave absorption effects in the microwires.

To address this outstanding issue, we have evaluated and compared the magnetic parameters, magneto-impedance, and microwave characteristics of glass-coated amorphous $Co_{64.63}Fe_{4.97}B_{16}Si_{11}Cr_{3.4}Ni_{0.02}$ (CoFeBSiCrNi) and $Co_{68}B_{15}Si_{10}Mn_7$ (CoBSiMn) microwires. We have found that the $Co_{68}B_{15}Si_{10}Mn_7$ microwire possessing a softer magnetic property shows a larger GMI effect and is a better microwave absorber for fabrication of a new class of FBG-based microwave energy sensor. Our study highlights a correlation between the magnetic softness, GMI, and microwave absorption effects in the microwires.
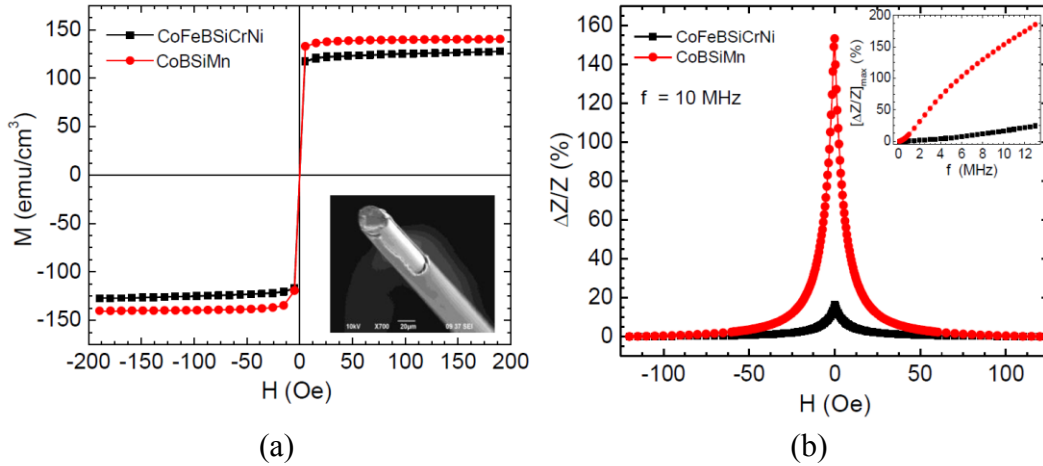

Figure 20: (a) Magnetic hysteresis loops of the CoFeBSiCrNi and CoBSiMn microwires. Inset shows a typical SEM image of a CoBSiMn microwire; (b) Magnetic field dependence of GMI ratio (ΔZ/Z) for the CoFeBSiCrNi and CoBSiMn microwires at f = 10 MHz. Inset shows the frequency dependence of the maximum GMI ratio ($[ΔZ/Z]_{max}$) for these microwires.

The glass-coated microwires were prepared by the glass-coated melt spinning technique and supplied by the MicroFir Tehnologii Industriale. The average diameter of the metallic core and the thickness of the glass-coating layer are determined to 25.2 μm and 3.1 μm for the CoBSiMn microwire and 14.2 μm and 2.8 μm for the CoFeBSiCrNi microwire, respectively. A typical scanning electron microscope (SEM) image in the inset of Figure 20(a) shows the morphology of a CoBSiMn microwire. The magnetic properties of the microwires were characterized by a vibrating sample magnetometer (VSM). The magnetoimpedance of the microwires was measured by a four-probe technique on a HP4192A impedance analyzer over a wire length of 1 cm at room temperature. A driving current of amplitude 1 mA over the frequency range of 0.1 – 13 MHz was supplied along the wire axis, in the presence of axial dc magnetic fields of up to ±120 Oe. At a given frequency, the GMI ratio was calculated by

$$\frac{\Delta Z}{Z} = \frac{Z(H) - Z(H)_{ref}}{Z(H)_{ref}} \times 100\% \tag{9}$$

where $Z(H)_{ref}$ is the impedance of a microwire taken as the reference to calculate the GMI ratio. In our case, the impedance at a maximum dc applied field (H = 120 Oe) was taken as the reference impedance. The microwire-based sensor probe was designed by attaching a microwire to an FBG cladding, which was then placed into a homemade 50 Ω microstrip transmission line, the so-called transverse electromagnetic (TEM) cell. Light from a broadband amplified spontaneous emission source (JDSU M/N BBS1560+1FP) was launched into an optical fiber that contained the FBG. Light transmitted through the optical fiber was monitored with an optical

28

spectrum analyzer (HP M/N 70951B). The TEM cell is comprised of two parallel copper plates with the geometry chosen to produce a 50 Ω impedance. As microwave energy of different frequencies and powers was sent through the transmission line, the optical spectrum transmitted by the FBG was recorded. The microwaves were generated by an HP M/N 8703A, amplified by a Mini-Circuits M/N ZHL-42W, and monitored with an HP M/N E4419B. The HP M/N 8703A was connected to the TEM cell via a coaxial cable which was terminated with a 50 Ω load. First, the microwave scattering parameter S11 due to a section of ordinary optical fiber was recorded as a reference scan. This reference scan was subtracted from an S11 scan taken with the sensor probe in the TEM cell. For the S11 scans, care was taken to not disturb the setup while the optical fiber was being moved.

Figure 20(a) shows the magnetic hysteresis (M-H) loops taken at 300 K for the CoFeBSiCrNi and CoBSiMn microwires. It can be observed that both the microwires exhibit a soft ferromagnetic characteristic, with extremely small coercivity ($H_c \sim 0.5$ Oe) and high saturation magnetization ($M_s = 125$ emu/cm^3 and 150 emu/cm^3 for CoFeBSiCrNi and CoBSiMn microwires, respectively). It is noted that while the effective anisotropy field is almost identical ($H_k \sim 10$ Oe) for both of the microwires, the M_s of the CoBSiMn microwire is much higher that of the CoFeBSiCrNi microwire. As we show below, this difference in the M_s of these microwires influences their GMI response and microwave absorption. Figure 20(b) shows the magnetic field dependence of GMI ratio ($\Delta Z/Z$) at a measurement frequency of 10 MHz for the microwire samples. The inset shows the frequency dependence of the maximum GMI ratio (i.e. $[\Delta Z/Z]_{max}$) for both types of microwire. It can be seen that the maximum GMI ratio is much higher for the CoBSiMn microwire than for the CoFeBSiCrNi microwire in the investigated frequency range of $0.1 - 13$ MHz. For instance, at $f = 10$ MHz $[\Delta Z/Z]_{max} = 153.32$ % for the CoBSiMn microwire, which is about 9 times higher than that for the CoFeBSiCrNi microwire ($[\Delta Z/Z]_{max} = 16.44$ %). To compare the field sensitivity of a GMI-based sensor using these two microwires, we have calculated the field sensitivity of GMI (η) for both the microwires at 10 MHz via $\eta = \frac{2\left[\frac{\Delta Z}{Z}\right]_{max}}{\Delta H}$, where ΔH is the full width at half maximum of a GMI curve. We find that the η for the CoBSiMn microwire ($\eta = 34.10$ %/Oe) is about 10 times higher than that for the CoFeBSiCrNi microwire ($\eta = 3.43$ %/Oe). This result indicates that the CoBSiMn microwire is better suited for use in magnetic field sensors. To quantify the impedance change of the transmission line due to the presence of each microwire as a microwave absorber, we first measured the S-parameter (S11) as a function of microwave frequency in the range of $0.1 - 7.5$ GHz. We then calculated the FBG wavelength (λ_{FBG}), which corresponds to the minimum of the observed S11 parameter, in response to microwave power delivered in the transmission line at various microwave frequencies. As an example, the variation in λ_{FBG} with microwave power for selected frequencies of 3.25 GHz and 5 GHz is depicted in Figure 21.
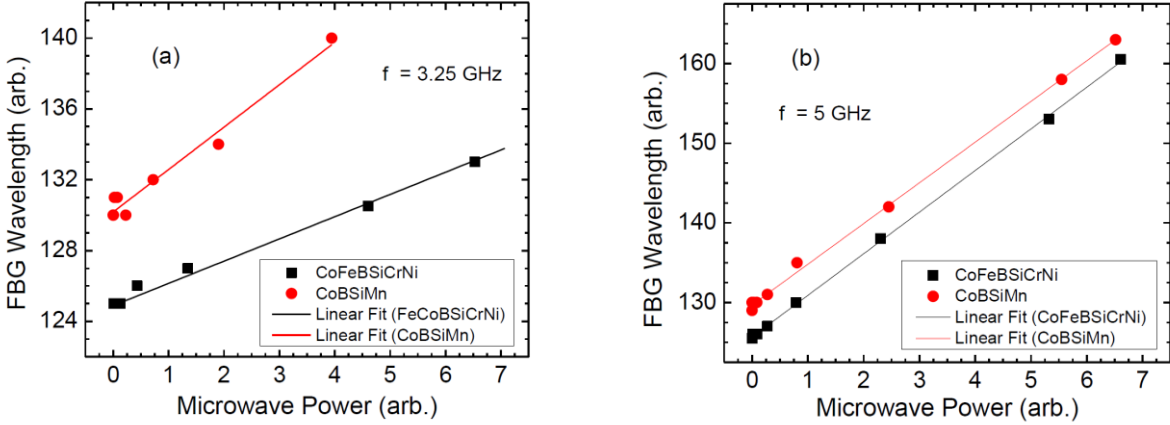
Figure 21: Bragg wavelength as a function of microwave power at two selected microwave frequencies of (a) 3.25 and (b) 5 GHz for the CoFeBSiCrNi and CoBSiMn microwires.

It can be observed that at a given frequency λ_{FBG} is shifted to a longer wavelength as the microwave power delivered to the microwave cell is increased. With increasing power, more of the microwave energy is absorbed by the microwire which begins to heat up, raising the temperature of the FBG and consequently shifting the λ_{FBG} to a higher value. The shift in λ_{FBG} increases linearly with the delivered microwave power at all frequencies. It is worth noting that in the investigated frequency range $0.1 - 7.5$ GHz, the slope of the λ_{FBG} shift with microwave power is significantly larger for the CoBSiMn microwire compared to the CoFeBSiCrNi microwire, from which it can be inferred that the CoBSiMn microwire will exhibit superior microwave energy field sensing capabilities. To confirm this, we have computed a figure-of-merit (FOM) at a particular frequency for each microwire probe using the following relation:

$$FOM = \frac{Linear\ slope\ of\ \Delta\lambda_{FBG}\ vs.\ microwave\ power}{10^{(S_{11}/10)}}. \tag{10}$$

The results of the FOM characterization of the microwire probes at various microwave frequencies are displayed in Figure 22. As expected, the probe using the CoBSiMn microwire as a heating element in the FBG sensor shows an improvement in FOM over the CoFeBSiCrNi microwire probe. Given that the thickness of the glass coating layer is almost identical for both types of wire (~ 3 μm) and that the measurements were carried out under the same conditions, the larger values of $[\Delta Z/Z]_{max}$, η, and FOM achieved for the CoBSiMn microwire are likely attributed to the softer magnetic property of the material. These results point to a correlation between the magnetic softness, GMI, and microwave absorption in the microwires.
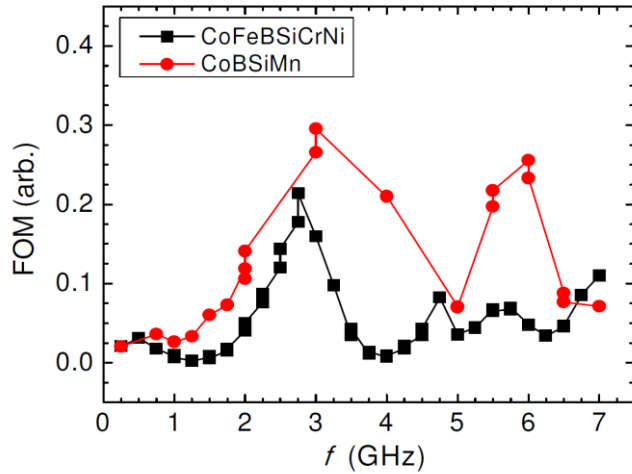

Figure 22: FOM of the microwire-based probes using the CoFeBSiCrNi and CoBSiMn microwires. The better performance of the probe using the CoBSiMn microwire is observed in the frequency range of $0.1 - 7$ GHz.

In summary, we have performed a comparative study of the magnetic properties, GMI and microwave absorption effects of two different types of glass-coated soft ferromagnetic amorphous microwires. We find that the larger GMI and microwave absorption effects achieved in microwires originate mainly from higher saturation magnetization, given that the coercivity, the effective anisotropy field, and the thickness of the glass-coating layer are the same. In addition to their existing applications in high-performance magnetic field sensors, the glass-coated soft ferromagnetic amorphous microwires can be exploited to be excellent microwave absorbers for the fabrication of FBG-based microwave energy sensors. The results have been published in *Journal of Applied Physics, 2014*.

2. A new type of multiwire-based sensors for magnetic sensing applications:

Recently, He *et al.* [26] have used a Co-based amorphous microwire as a sensor core to improve sensitivity to a level that allows the relatively weak magnetic signals of a magnetic system to be detected. In this design the change in the inductance of the coil-system is driven by an ac current in the presence of an external dc magnetic field along the axis of the coil, producing a longitudinally excited magneto-inductance (LEMI) effect. There is a need for improved sensitivity in LEMI-based sensors in order to fulfill the increasing requirements of industrial and engineering applications.
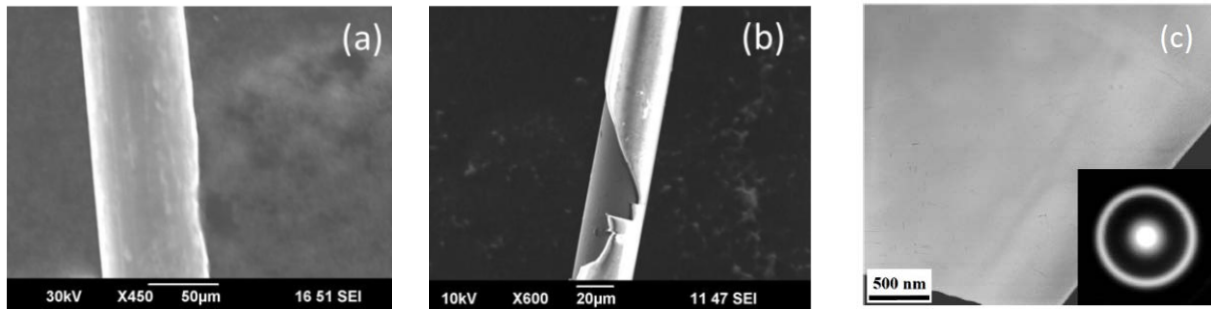

Figure 23: SEM images of (a) a melt-extracted $Co_{68.2}Fe_{4.3}B_{15}Si_{12.5}$ microwire and (b) a glass-coated $Co_{68}B_{15}Si_{10}Mn_7$ microwire; (c) a TEM image of the $Co_{68.2}Fe_{4.3}B_{15}Si_{12.5}$ microwire, with the corresponding SAED pattern shown in the inset.

We have proposed an effective approach to improve the sensitivity of inductance coil sensors by designing a sensor core that consists of multiple soft ferromagnetic microwires. A systematic study of the LEMI effect has been performed in a non-magnetic copper wire coil with a filler composed of multiple Co-rich amorphous microwires. Melt-extracted microwires (MEW) of $Co_{68.2}Fe_{4.3}B_{15}Si_{12.5}$ and glass-coated microwires (GCW) of $Co_{68}B_{15}Si_{10}Mn_7$ with excellent soft magnetic properties were used for this study.

Figure 23 shows the SEM images of the MEW and GCW, along with a TEM of the MEW. SEM images taken on different segments of wire showed an average diameter d of ~50 μm for the MEW and ~25 □m for the G TEM and SAED data confirm the amorphous nature, morphology, and quality of the prepared microwires.
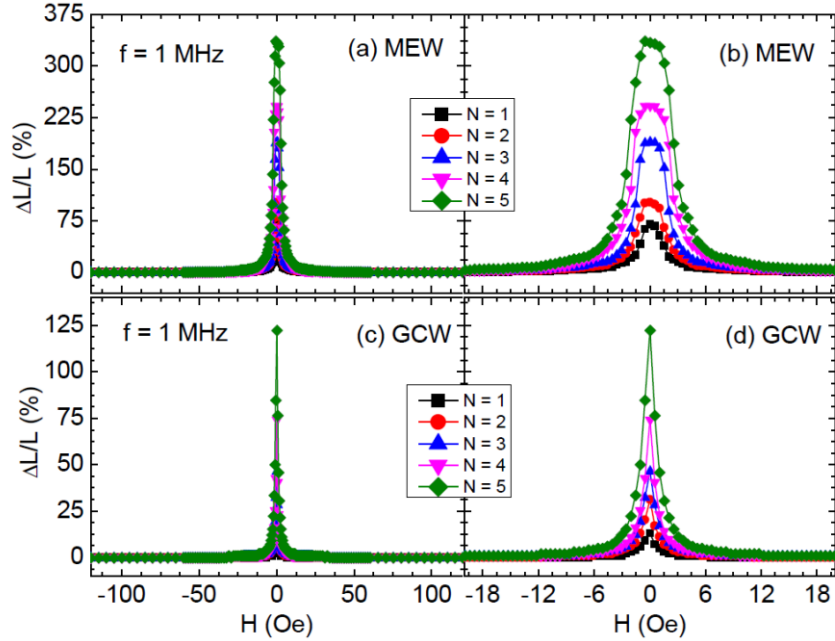
Figure 24: Magnetic field dependence of the inductance (*L*) of the coil measured at *f* = 1 MHz for (a, b) the MEW based core and (c, d) the GCW based core for N = 1 - 5. (b) and (d) show the enlarged portions of (a) and (c), respectively.

We have shown that the LEMI ratio and field sensitivity of an inductive coil depend strongly upon the filler-to-air ratio inside the coil, the magnetic softness, and the anisotropy axis distribution of the microwire. Relative to a single-microwire based sensor, the LEMI ratio and field sensitivity of a multi-microwire based sensor are enhanced by 3 to 4 times, when varying the number of microwires inside the inductive coil. The sensitivity of the sensor using four glass-coated $Co_{68}B_{15}Si_{10}Mn_7$ microwires in the core reaches a maximum value of 1957 %/Oe. Figure 24 shows the magnetic field dependence of the LEMI ratio ($\Delta L/L$) at a representative frequency of 1 MHz for both systems of wire. The LEMI ratio for N = 1 is 71.68 % (13.04 %) for the MEW (GCW) and increases with N to reach 337 % (122 %) for N = 5. From a sensor application perspective, the large enhancement of the LEMI ratio achieved for the sensor core composed of multiple soft ferromagnetic wires (as compared to that of a single wire) is ideal for developing highly sensitive magnetic sensors for detection of weak magnetic fields in engineering and biological systems. We have also found that the increase in [$\Delta L/L$]$_{max}$ with N was very large in the frequency range 0.1 MHz – 2 MHz and became less prominent at high frequencies (*f* > 2 MHz). This indicates that the frequency range of 0.1 MHz – 2 MHz would be the most suitable choice for the operating frequency of sensors based on the LEMI/magnetic-wire-core design in this study.

In summary, we have developed a novel method of improving the sensitivity of LEMI-based inductance coil sensors by designing a sensor core that consists of multiple soft ferromagnetic microwires. The effects of magnetic softness and anisotropy distribution of Co-rich amorphous microwires, as well as the filler/air ratios on the LEMI ratio and field sensitivity of an inductive coil are elucidated. Our study paves a pathway for the development of novel room-temperature electric contact free magnetic sensors for use in industry, biomagnetism, space science, and geoscience. The main results of the work have been submitted for publication in *Journal of*

Applied Physics, 2014. Further research is being performed to optimize the sensitivity of this type of sensor for biodetection.

3. A new type of magneto-reactance based biosensor for detection of cancer cells and biomolecules

A combination of the GMI effect with functionalized magnetic nanoparticles (MNPs) has high potential for the development of a simple and reliable biosensing system that can be used as a quick detection technique before magnetic resonance imaging (MRI) [27]. Recently, we have demonstrated the high capacity of detecting low concentrations of ~10 nm SPIO MNPs and biomolecules tagged to them using a magneto-reactance (MX) based biosensor [28-30]. The detection sensitivity of the MX-based biosensor has been reported to reach an extremely high value of 30%, which is about 4 times higher than that of a MI-based biosensor [30].

In this study we demonstrate the capacity of detecting magnetically weak manganese oxide (MnO) nanoparticles and the Lewis lung carcinoma (LLC) cancer cells that have taken up these nanoparticles using a novel biosensor based on the MX effect of a soft ferromagnetic amorphous ribbon with a micro-patterned surface.
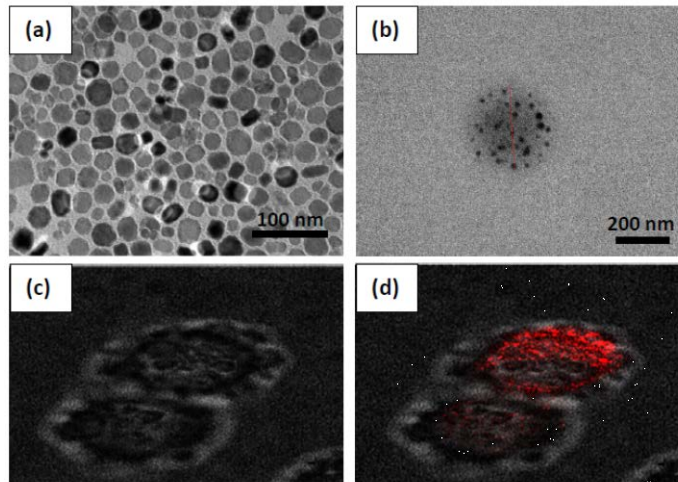

Figure 25: TEM images of the MnO MNPs (a) and MLMNs (b); Optical images of the LLC cells (c) and LLC cells that have taken up the MLMNs (d).

MnO nanoparticles and MnO MNPs incased in phospholipids (Manganese Oxide Lipid Micellar Nanoparticles or MLMNs) were prepared as described previously in the work [31]. Dichloromethane was added to improve the dispersibility of the nanoparticles. The nanoparticles were washed three times in acetone to remove excess surfactant and solvent. To encapsulate MnO nanoparticles, PEG-2000 PE, DC-cholesterol, and DOPE were added to chloroform and MnO nanoparticles were added to the solution. The chloroform was then evaporated in a vacuum oven and the dry film was heated at 80 °C. Water was added to the dry film and the solution was sonicated. For cell uptake experiments the MLMNs were labeled with DOX as a fluorescent marker. Doxorubicin hydrochloride (DOX) along with 4 M equivalents of triethylamine was added to chloroform and the mixture was sonicated to dissolve the DOX. Phospholipid micelles encapsulating DOX and MnO (DMLMNs) were prepared as previously described with some

modifications. Cellular uptake of MLMNs for the MnO detection experiments was preformed in the same manner as those of the FMLMN uptake studies. Cells were seeded 24 h prior to transfection into a 35mm dish in 2ml of complete medium (DMEM containing 10% FBS, 2 mM L-glutamate and 1% penicillin/streptomycin). At the time of MLMNs addition, the medium in the dish was replaced with 1.5ml of fresh DMEM without FBS. Two milligrams of MLMNs, diluted in 50 μl DMEM with no FBS, was added the dish. After 24 h of incubation the cells were collected off of the dish using 0.25% trypsin and counted. Various dilutions of the cells were prepared for the impedance measurments. Various dilutions of the MLMNs alone were also prepared for the impedance measurments. The magnetic hysteresis loop (M-H) of the MnO MNPs was measured at room temperature by a vibrating sample magnetometer (VSM).

Figure 25(a,b) shows the TEM images of the MnO MNPs and MLMNs. Figure 25(c,d) shows optical images of the blank LLC cells and the LLC cells that have taken up the MLMNs. TEM images of MnO MNPs showed spherical nanoparticles with a size range of 10 – 30 nm. Analysis by dynamic light scattering (DLS) gave the hydrodynamic radius for the M-LMNs to be about 100-200 nm, which was confirmed by TEM images. Cellular uptake of the MLMNs was examined by labeling the particles with DOX. LLC cells were incubated with the DMLMNs for 4 h and the DOX was visualized by confocal microscopy (Fig. 25(d)). DMLMNs were seen in the cytoplasm surrounding the nuclei of the cells.

Figure 26 shows the magnetic hysteresis (M-H) loop of the MnO MNPs measured at room temperature, with an inset showing an enlarged portion of the low-field loop. From the main panel of Fig. 26, it appears that the MnO MNPs behave like paramagnetic particles whose magnetic moments often increase linearly with respect to an applied magnetic field. However, the inset of Fig. 26 shows a small hysteresis with a coercivity of $H_c \sim 50$ Oe and a remanence magnetization of $M_r \sim 2.5 \times 10^{-3}$ emu/g in the low field range (± 100 Oe), which is characteristic of a weakly ferromagnetic material. These small values of M_r and H_c indicate a reversible magnetization process when the magnetic field is recycled. Such a behavior of the MnO MNPs is similar to that of superparamagnetic Fe_3O_4 MNPs, except that the former has a much smaller magnetic

Figure 26: Magnetic hysteresis loop (M-H) of the MnO MNPs taken at room temperature.

moment compared to the latter. In other words, a magnetic biosensor with higher detection sensitivity would be needed for detection of the MnO MNPs and the LLC cells that have taken up these MNPs.
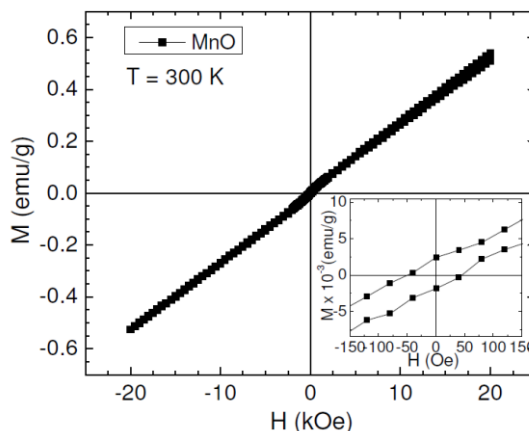
Figure 27(a) and (b) show the field dependence of MI and MX ratios measured at f = 1.5 and 0.5 MHz, respectively for the etched ribbon with 10   □l of LLC, N drop-casted on the ribbon surface. The operating frequencies for the MI and MX-based detection were chosen to be f = 1.5 and 0.5 MHz as the highest detection sensitivities were respectively achieved at these frequencies.[2] As one can see clearly in Fig. 27(a,b), the MI and MX profiles

have a double-peak feature for all the samples. This double-peak feature has been typically attributed to the presence of transverse anisotropy in a Co-based ribbon. It has been shown that the peak position corresponds to the effective anisotropy field of the ribbon[5]. The MI and MX ratios were first measured with and without the blank LLC cells at the desired frequencies, showing a negligible influence of the cells on the MX or MI signal. The measurements were then repeated for equal volume and concentrations of the MLMNs and the LLC cells that have taken up the MLMNs. It is worth noting in Fig. 27(a) that neither the MLMNs-embedded LLC cells nor the MLMNs themselves altered the MI ratio of the ribbon. However, the MX ratio of the ribbon was found to increase significantly in the presence of the MLMNs and the LLC+MLMNs (Fig. 27(b) and its inset).
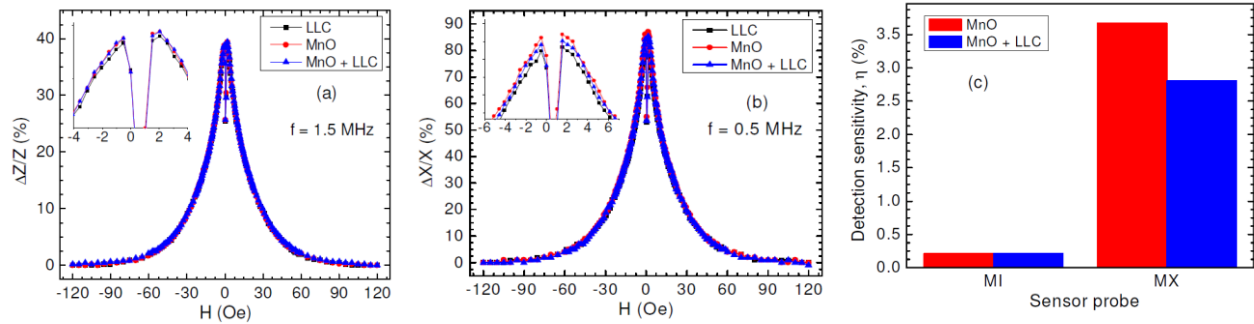

Figure 27: Magnetic field dependence of $\Delta Z/Z$ (a) and $\Delta X/X$ (b) ratios with LLC, MnO MNPs, and MnO-embedded LLC cells at f = 0.5 and 1.5 MHz, respectively; (c) A comparison of the detection sensitivity between the MI and MX sensor probes for detection of the MLMNs and MLMNs-embedded LLC (0.05mg/ml MnO and 8.25 x 10^4 cells/ml respectively).

To better illustrate the detection capacity of the MLMNs and the LLC cancer cells that have taken up the MLMNs, we have evaluated the detection sensitivity of the sensor using Eq. (3). The results are plotted in Figure 27(c). It can be seen that the MI ratios for both MLMNs and LLC+MLMNs reached at a similar level which is slightly higher (< 0.4%) than the LLC level. This indicates that the MI-based biosensor is not suitable for probing the MLMNs and the MLMNs-embedded LLC cells at the tested concentrations. However, the detection sensitivity reached much larger values of ~ 3.6% and 2.8 % for the bare MLMNs and the MLMNs-embedded LLC cells, respectively.

The variation in the original MX ratio of the ribbon due to the presence of the MLMNs and the MLMNs-embedded LLC cells can be explained by considering the disturbance of the applied dc longitudinal and ac transverse fields due to the presence of the fringe fields of the MLMNs on the surface of the ribbon. Although the magnetic moments of the MLMNs are small, microholes produced by the etching technique on the ribbon surface minimize their physical motion and make a stronger field disturbance effect. As a result, the MX value of the ribbon changes in the presence of the MLMNs or the LLC cells that have taken up these MLMNs. The detection sensitivity due to the presence of the MLMNs-embedded LLC cells is smaller than that obtained for the MLMNs themselves. This decrease in η can be explained by considering the fact that the effect of fringe fields decreases as the distance from the MLMNs to the ribbon surface is increased. In the present case, when the MLMNs are embedded in the LLC cells, the distance

from the MLMNs to the sensor surface increases. As a result, the magnetic disturbance effect becomes weaker, leading to a lesser influence on the original MX value of the ribbon.

In summary, we have demonstrated the capacity of detecting magnetically weak manganese oxide (MnO) nanoparticles and the Lewis lung carcinoma (LLC) cancer cells that have taken up these nanoparticles using a novel MX-based biosensor. While the magnetic moment of the MnO nanoparticles is relatively small, and a magneto-impedance based sensor fails to detect them in solution (0.05mg/ml MLMNs) and inside cells at low concentrations (8.25×10^4 cells/ml), the detection of these nanoparticles and the LLC cells containing them is achieved with the MX-based sensor, which respectively reaches the detection sensitivity of ~3.6% and 2.8% as compared to the blank cells. Since the MnO nanoparticles are a promising contrast agent for magnetic resonance imaging (MRI) of lung cells, the MX-based biosensing technique can be developed as a pre-detection method for MRI of lung cancer cells. The main results of the work have been accepted for publication in *Journal of Applied Physics*, 2014.

Formation and delivery of functionalized artificial platelets for rapid cessation of internal bleeding.

Traumatic injuries such as amputations and internal bleeding continue to plague the battlefield soldier. The body's own ability to stop bleeding is ineffective at correcting such injuries. Tourniquets can cause necrosis. Platelet transfusions and clotting factors can cause undesirable immune responses and thrombosis (e.g. stroke) in the body. Recently, researchers have successfully tested an artificial platelet (see Figure 28) which is biocompatible and reduces bleeding times significantly [32]. However, these artificial platelets still pose a risk for thrombosis in the body; they may form a clot in a part of the body that is not near the wound.
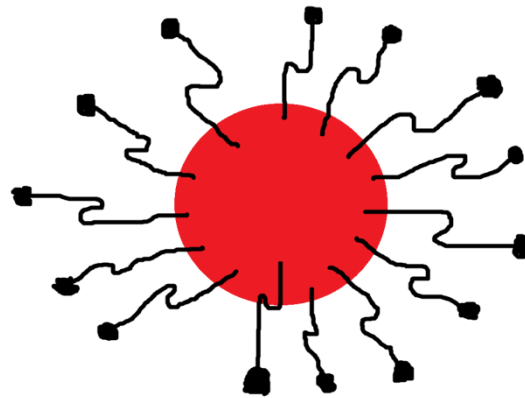

Figure 28: Schematic depiction of an Artificial Platelet. The core is made of poly(lactic-co-glycolic acid)-poly-L-lysine (PLGA-PLL). Conjugated to the core are the arms, which are made of polyethylene glycol (PEG). The PEG arms are terminated with functionalities which serve the purpose of attaching to natural platelets already found in the blood.

The aim of this project is to design a biocompatible package that will deliver the artificial platelets and other hemostatic accelerants (i.e. adenosine diphosphate, ADP) only to the area of the body in proximity to the wound. There have been some efforts to encapsulate magnetic nanoparticles within a polymer so that the composite capsules can be guided with a magnetic field through the body [33-38]. We intend to achieve this with a bio-compatible polymer that undergoes a sol-gel transition at a temperature that is few degrees above the body temperature (38°C) to release its contents. Encapsulation of magnetic particles within poly(N-isopropylacrylamide) (PNIPAM) via a process known as emulsion polymerization [34,35,38] has been attempted to create a temperature

sensitive drug-delivery system. The finished delivery system will be injected intravenously into an injured soldier. An externally applied magnetic field near the wound site will facilitate the accumulation of the capsules near the wound as the circulatory system moves the medicine around the body. After enough time has passed to ensure all of the medicine has collected near the wound site, application of an external RF field is expected to raise the temperature of the capsule above the transition temperature via the magnetic nanoparticles, thus releasing its contents.

Poly(N-isopropylacrylamide) as a Polymeric Drug Delivery Nanocapsule

In order to achieve the goal of the project, we attempted to synthesize a polymeric "envelope", composed of PNIPAM, which will encapsulate the artificial platelets, hemostatic accelerants such as adenosine diphosphate (ADP), and Fe_3O_4 magnetic nanoparticles. A schematic diagram of the system is illustrated in Figure 29. The artificial platelets and ADP will function to facilitate hemostasis. The magnetic nanoparticles will serve to both guide the entire system to the wound via a magnetic field and to heat the system, releasing its contents, after being exposed to an RF field. This section describes the properties of PNIPAM that led to it's choose for the polymeric envelope.
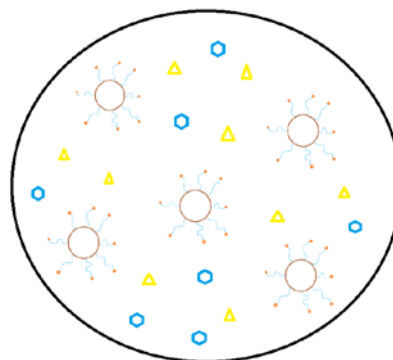

Figure 29: Included within the polymeric shell of PNIPAM are the artificial platelets, magnetic nanoparticles (hexagons), and hemostatic accelerants (triangles). Hemostatic accelerants such as adenosine diphosphate are already involved in natural hemostasis. The body releases these compounds to promote the cessation of bleeding.

"Smart polymers", like PNIPAM, are those that respond to stimuli such as temperature or pH changes. Many polymers are known to exhibit a response to external stimuli. However, the choice of such smart polymers that are bio-compatible are limited. [34, 35]. A biocompatible smart polymer of particular interest to researchers is PNIPAM. The reason this polymer is the focus of so much attention is that it undergoes a sol to gel phase transition near the average temperature of the human body, making it particularly useful in biomedicine. Turning this polymer into a vehicle for controlled drug delivery is an active research field [34, 35]. The monomer of PNIPAM is NIPAM and it has the molecular structure shown as in Figure 30. This molecule is known to stretch itself out below its lower critical solution temperature (LCST) of about 33°C allowing it to bond more readily with water. At lower temperatures the enthalpy term dominates the molecule's statistical mechanics
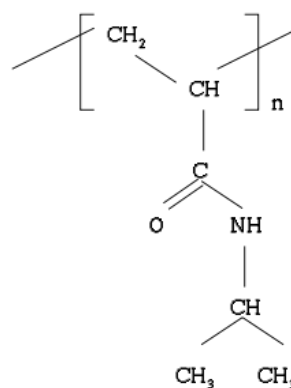

Figure 30: Molecular structure of a single unit of PNIPAM.

making it hydrophilic. Macroscopically, this means a sample of aqueous PNIPAM is a gel below the LCST. Above the LCST the molecule pulls in on itself bonding with less water. When temperatures are greater than 33°C the entropy term dominates making the molecule hydrophobic. On a larger scale an aqueous PNIPAM sample changes to a free flowing solution when the temperature is increased [34-36]. This transition from gel to sol, upon heating past the LCST, is what will allow us to "deliver the package" to the targeted wound site as discussed in the next section.

Design of the platelet delivery system

This project focusses on two different techniques for designing the polymeric capsules in the size range of ~200-500 nm; (1) Emulsion polymerization, where nano-gel particles are formed by combining a monomer and a polymerizing initiator. This process is fairly simple, but control of the nano-gel sizes and incorporation of bio molecules and magnetic nanoparticles may be challenging. However, if successful, it will simplify the growth process. (2) Nebulization of the polymer solution to form droplets followed by manipulation of the polymer concentration in the droplet to form the gel capsules with desired size. This report presents initial results on PNIPAM nano-gel particles synthesized by emulsion polymerization.

A polymeric particle that forms via crosslinking of the adjacent linear polymeric chains to connect to one another at various places via covalent bonds, forming a sphere like vessel [17, 18] was envisioned. In this way, a drug can be loaded at low temperature, in the expanded state of the molecule, which translates into a swollen particle. Once stimulated in the body, the temperature increase would cause the capsule to shrink, thus squeezing the drug through the mesh-like crosslinking network [38].

The particles are synthesized through a process called emulsion polymerization. This technique involves adding the monomer, NIPAM, to a stable emulsion containing initiator molecules,2-2'-azobis-(2-amidinopropane hydrochloride), which begin the polymerization process. Particles are typically synthesized at 70°C. The atmosphere above mixing chemicals is usually purged with nitrogen to remove oxygen. Polymerization occurs in regions of the solution protected by an additional surfactant molecule. All this happens in the liquid phase. In the case of PNIPAM a crosslinking agent, methylenebisacrylamide, is also present [38].
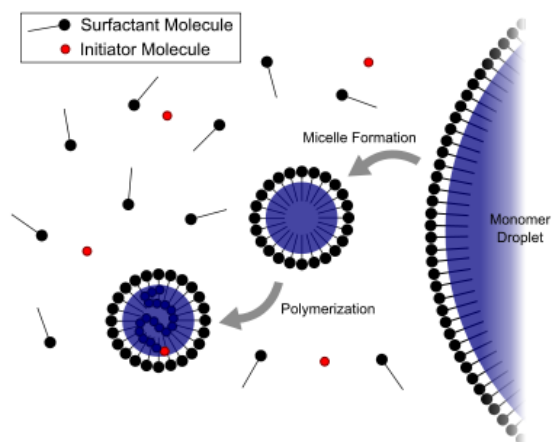

Figure 31: Schematic of the emulsion polymerization process. [39]

Figure 31 shows how the droplets are formed during the emulsion process. The figure evolves in time from right to left. When the monomer is added to the water, large droplets of it are protected from the water by the surfactant (hence the reference to emulsion in the name). The surfactant molecules form micelles and the monomer begins to diffuse through the water into the micelles. The initiator tends to react only within the smaller micelles rather than the

larger monomer droplets due to the difference in surface area. The monomer polymerizes within the micelles and terminates giving us the polymer particles. Crosslinking agents are necessary to yield the mesh-like feature discussed above. The monomer droplets continue to give up their contents to the micelles, shrinking in size while the micelles grow. Given enough initiator molecules, the monomer droplets will eventually vanish. In this way it is easy to see how the size of the polymer particles can be controlled with the amount of initiator in the solution. [34, 38]. Our first step out of two was to carry out the details listed above, exactly as described, to synthesize simply the polymeric envelope without any contents. In our second step we introduced the magnetic nanoparticles into the polymerization process so that they would be taken up by the micelles in a seeding process.

Microscopic characterization of PNIPAM polymeric spheres, magnetic nanoparticles, and PNIPAM polymeric spheres encapsulating magnetic nanoparticles was carried out with high resolution transmission electron microscopy (TEM-HRTEM, FEI Tecnai F20 S-Twin TEM). Dynamic light scattering (DLS) studies were conducted with Malvern Instruments Zetasizer Nano S Model ZEN1600 for determining particle size distributions. After emulsion polymerization, the product was dialyzed and centrifuged at 10,000 rpm for 15 minutes for TEM sample preparation following reported recipes [38]. After centrifugation, the samples were dried through lyophilization (freeze drying) so that the solute can be weighed and redisposed in a known amount of DIW, thus determining the concentration of the sample. TEM samples were prepared by placing one or two drops of the dispersed liquid onto a coated copper grid. After air drying, a single drop of uranyl acetate stain was deposited in the same manner and allowed to air dry. The stain served to bring out details in the PNIPAM particles that would otherwise go undetected.
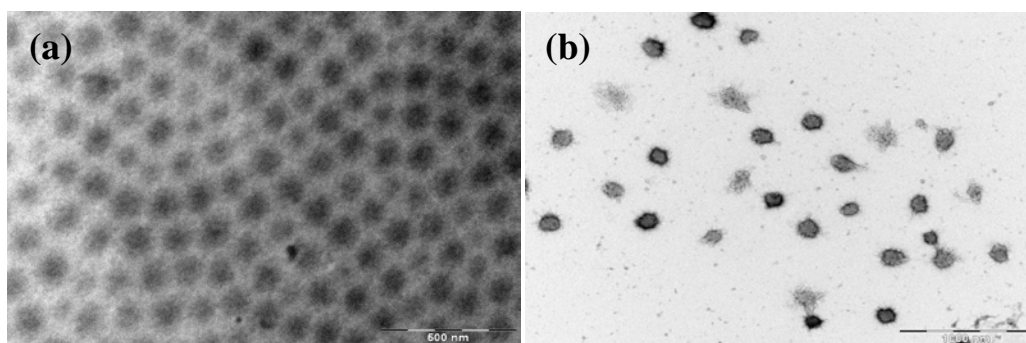

Figure 32: (a) TEM image of 0.5 wt. % PNIPAM particles after dialysis, but prior to centrifugation. Agglomeration of PNIPAM particles can be observed. (b) TEM image of PNIPAM particles in 1.0 wt % concentration aqueous solution after centrifugation showing no agglomeration.

PNIPAM particles synthesized by emulsion polymerization were characterized as-grown as well as after a centrifugation process to remove unreacted initiator and excess surfactants. Figures 32 (a) and (b) show TEM images of the PNIPAM particles before and after the centrifugation, respectively. Figure 32 (a) shows a fairly uniform particle size distribution and self-assembly of the gel particles in presence of the surfactant. Removal of surfactants did not lead to agglomeration and stayed as distinct particles, perhaps due to the micelle nature of the gel

particles. The un-agglomerated particles shown in Figure 32 (b) are ~150 nm in average diameter.

Figure 33 shows the temperature profile of the particle size distribution of PNIPAM particles measured using DLS. A shrinkage in particle size with increasing temperature is observed from the analysis. From Figure 33 it can be seen that the particles have an average size of 300 nm at 20 ºC, (orange color curve) however when heated to 50 ºC they reduce in size to less than 100 nm (blue curve), indicating gel-to-sol transition. On the other hand, the process is thermally reversible where it was observed that the particles regained their size when cooled to 20 ºC. This property is significant for the effectiveness of PNIPAM as a drug-delivery system.
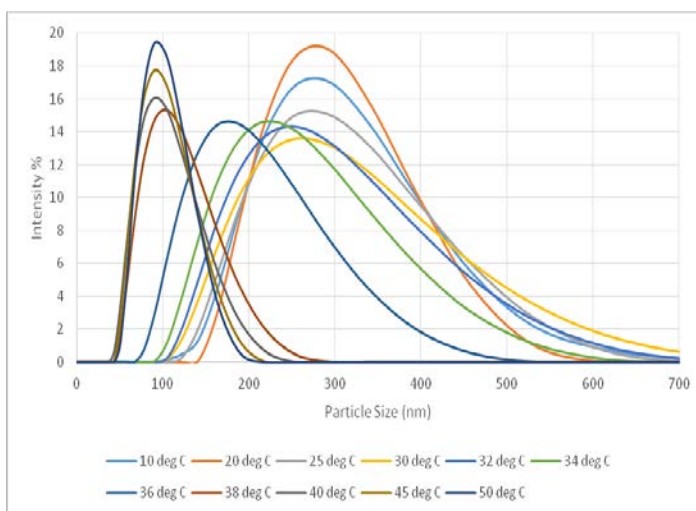

Figure 33: DLS data showing the temperature profile of the particle size distribution of PNIPAM particles.

Figure 34 (a) shows a representative TEM image of the as-prepared Fe_3O_4 nanoparticles. From the image an average particle size of 11 nm was estimated. Once the magnetic nanoparticles were encapsulated within the PNIPAM polymeric envelope images like that in Figure 34 (b) were obtained with TEM. Shown here is a single polymeric nanoparticle encapsulating many magnetic nanoparticles. The entire system shown here is about 166 nm in its longest dimension.
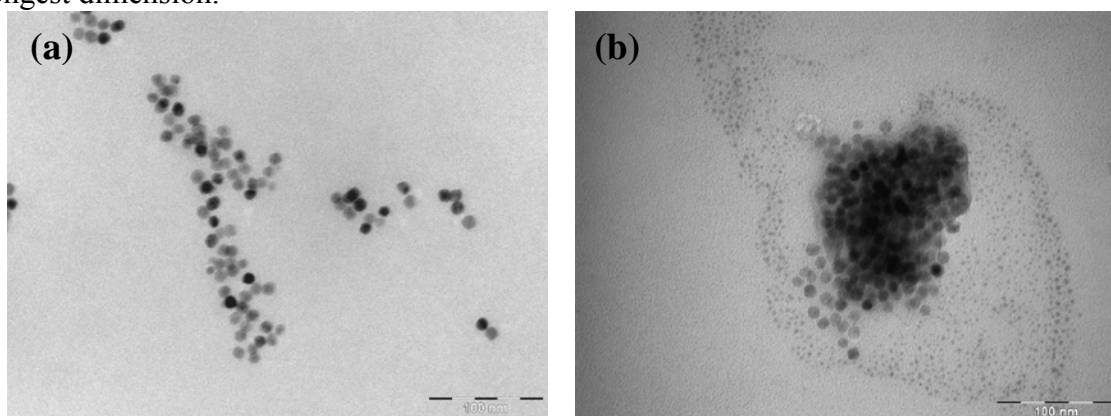

Figure 34 (a). Iron oxide magnetic nanoparticles. (b) PNIPAM polymeric envelope containing the magnetic nanoparticles meant for guidance and heating.

Emulsion polymerization of the temperature tunable polymer PNIPAM was successful in synthesizing nano-gel particle. However, controlling the particle size was found difficult. Furthermore, even though magnetic nanoparticles were incorporated into the gel by having the magnetic nano particles in the starting monomer solution, controlling the density of particles in

each nano-capsule and complete containment of the magnetic particles was difficult. We have initiated the second growth technique and hope to report results in the next quarterly report.

Investigation of the Transition Temperature of poly (N-isopropylacrylamide)

Efforts to encapsulate magnetic nanoparticles within poly(N-isopropylacrylamide) (PNIPAM), through a process called emulsion polymerization, were detailed earlier [37, 38]. A description of the chemistry behind synthesizing these capsules, their characterization, and results was provided. Here, an in-situ transmission study of phase transition of PNIPAM using remote RF heating of Fe_3O_4 nanoparticles is presented. The effects of RF heating on aqueous solutions of PNIPAM and Fe_3O_4 nanoparticles to observe phase transitions of PNIPAM were carried out. Remote heating of PNIPAM encapsulated molecules is crucial for targeted drug delivery using temperature-sensitive polymeric hosts. It is desirable to know how the thermo-responsive polymer will react to this stimulus. In particular, the aim of this study is to investigate what role, if any, polymeric concentration has on its lower critical solution temperature (LCST) [33-35].

PNIPAM (average M_n 10,000) was used as received from Sigma Aldrich. Magnetite, Fe_3O_4 nanoparticles (15-20 nm) (MNPs) were used as received from US Research Nanomaterials Inc. These solutes were dispersed in de-ionized water (DIW). Solutions were prepared by pouring weighed solute into empty storage vials and then pouring in known volume of DIW thus giving the desired concentration. The solutions were then ultra-sonicated until fully dispersed.

Figure 35 shows a schematic diagram of the experimental setup. The prepared solutions were placed into an optical-plastic cuvette. The cuvette was suspended so that it is coaxial within the RF heating coils. A He-Ne laser is angled so that it can pass between the coils, through the sample cuvette, between the coils again, and incident on a photoresistor, whose resistance was measured using a Keithley multimeter. A computer-controlled LABVIEW program was used to record a 2D array of resistances along with the corresponding time during the experiment.
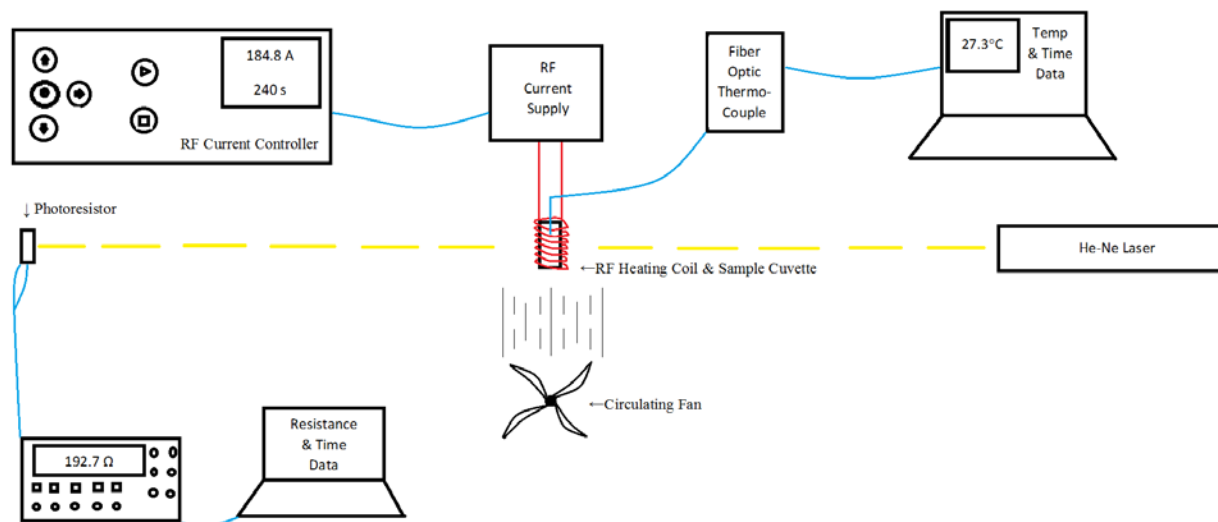

Figure 35: Experimental setup of optical studies of aqueous PNIPAM containing MNPs

Meanwhile, the RF current controller sent signals to the RF current supply that dictated how much current passed through the coils and for how much time. A fiber optic thermocouple was used to monitor the temperature in the sample cuvette. A fiber optic cable is necessary since the RF heating equipment would melt the metal in a conventional thermocouple. Temperature data is recorded by an attached computer along with the elapsed time of the experiment. A circulating fan is necessary in order to prevent convective heating of the sample. Only heating due to RF stimulation of MNPs is of interest. The need for the circulating fan is justified in the next section.

The RF system used is an EasyHeat Induction Heating System LI Model 3542 by Ambrell. This technology will be used to stimulate the capsule to deliver its clotting contents to the wound site. It works by sending an AC current through its coils. The coils are water cooled in order to protect the equipment and to reduce convective heating of the sample. The changing current gives rise to a magnetic field along the axis of the coils according to the equation

$$H = \frac{NIa^2}{\left[2(z^2 + a^2)^{\frac{3}{2}}\right]}$$

Here H is the magnetic field strength, N is the number of loops in the coil, I is the current, a is the radius of the coil, and z is the distance from the center of the coil. Obviously, the strength of the field is a function of the distance from the center of the coil and is represented in Figure 36. The field stimulates the MNPs to heat up the sample they are dispersed in.
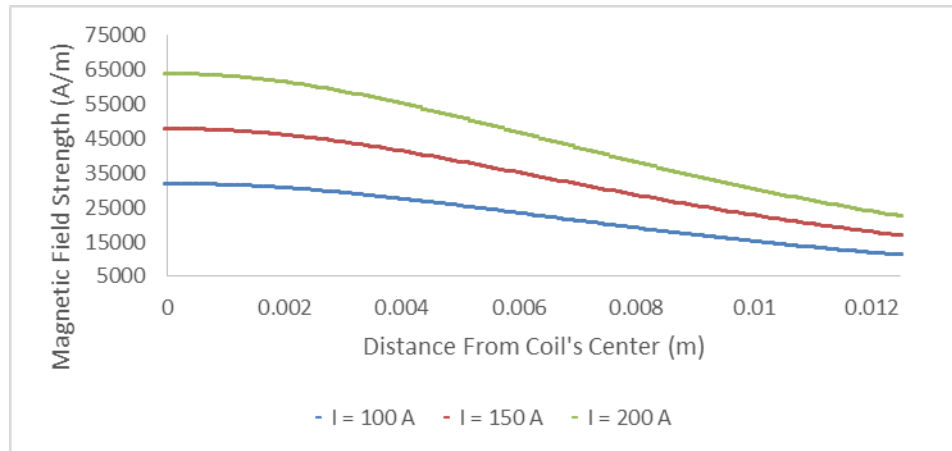

Figure 36. Magnitude of RF field as a function of the distance from the center of the coil

Prior to conducting the study of aqueous PNIPAM containing MNPs it was necessary to characterize the RF system. First, a study was performed to determine what effect the system had on a sample of DIW alone. Next, RF heating trials were carried out on MNPs in DIW. Finally, samples of PNIPAM with MNPs were prepared and used to carry out the described experiments.

It was initially thought that DIW should show no temperature response during RF heating trials under any applied current. If the DIW sample contains no MNPs then there should be no response to an applied RF field. As stated in the previous section the RF coils are water cooled. The manufacturers of the equipment flow water throughout the RF equipment, including coils, to maintain safe operating temperatures. They also claim this water flow is sufficient to prevent convective heating of the sample.

Figure 37: Heating curve for DIW subjected to RF heating.

Figure 37 shows that the water flowing through the RF coils is not sufficient to prevent convective heating. Approximately, 3 mL of DIW was subjected to 10 trials each corresponding to applied currents of nearly 200 A, 150 A, and 100 A. This graph is the resulting average heating during 5 minute trials. At all three applied currents the samples did heat thus demonstrating the need for further cooling of the sample. As stated before, only RF heating, not convective heating, is of interest.

Figure 38. Change in temperature as a function of time for DIW with vertical cooling fan.

To prevent convective heating a small fan was employed to circulate the air in and around the RF heating coil. The fan was positioned directly under the sample and coil so that its direction of air flow was vertical and upward. Several different fan distances from the bottom of the sample and coil were tested to optimize the setup.
Note the smaller change in temperature when comparing Fig. 37 to Fig. 38. From this point on it should be assumed that trials were run with the vertical fan in place. It is interesting to note that the sample initially cooled due to the fan. Then the sample warmed due to convective heating.
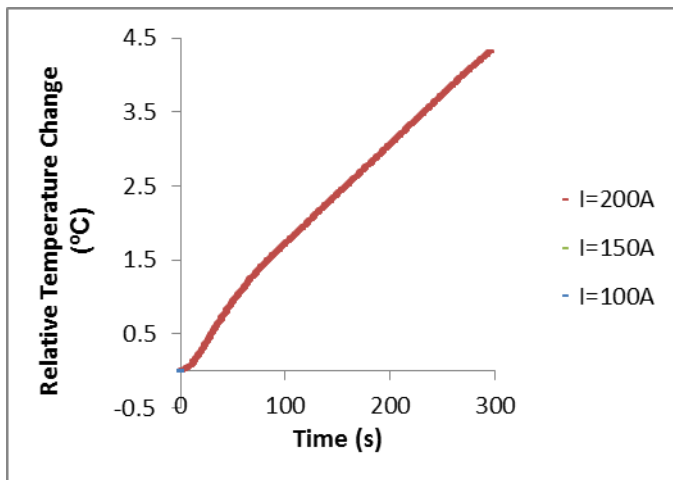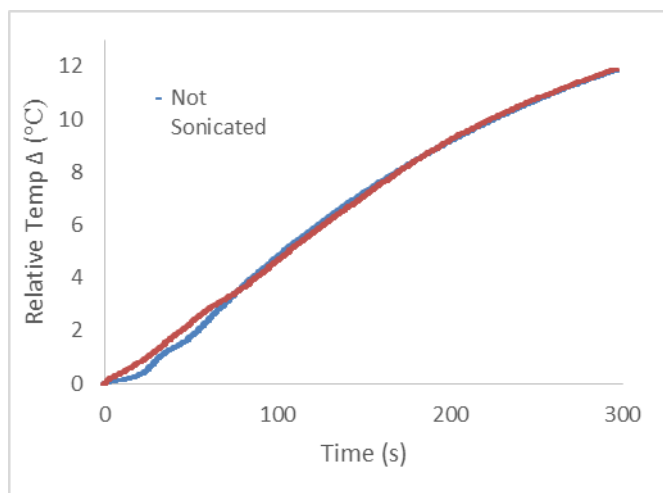

Figure 39. Comparison of dispersed versus settled MNPs.

43

RF Heating of MNPs and DIW

Once the question of the source of heating was solved the next question was the importance of dispersed MNPs. That is to say, do homogenously distributed MNPs heat a sample differently than MNPs that have settled at the bottom of the cuvette? To test this multiple trials were conducted on two samples. Everything about the samples and trials was kept constant except for the nature of how the MNPs were dispersed. In one sample the MNPs were allowed to settle to the bottom and special care was taken not to disturb them. In the other, the sample was ultrasonically agitated constantly just prior to the start of the trial. Each sample had 10 trials performed on it at a current of nearly 200 A. The data was averaged and the results are given in Figure 39 below. The plot indicates that there is no significant difference between keeping the MNPs well dispersed and allowing them to settle to the bottom.

RF Heating of PNIPAM, MNPs, and DIW

With the system characterized, optical studies on the thermoresponsive polymer are now possible. Samples having a volume of 3 mL were prepared for PNIPAM concentrations of 0.2, 0.3, 0.4, 0.6, 0.8, 1.0, and 1.2 weight %. All samples studied thus far had an amount of Fe_3O_4 MNPs (15-20 nm) added to the sample making it 2 mg/mL in concentration. A fan was used, as shown in Figure 35, to reduce convective heating. The MNPs were allowed to settle overnight, or in some cases a magnet was used to draw the MNPs quickly to the bottom of the cuvette. It turns out settled MNPs are crucial when studying polymeric solutions with this technique. If the MNPs are not settled then the laser is obscured. When studying a single concentration 10 trials are run and the results are averaged and error identified as standard deviation. Two sets of data are generated, in the form of a two dimensional array, for a single concentration. One set of data, temperature versus time, is taken by the fiber optic thermal probe's accompanying software. The other data set, photoresistance versus time, is taken by a Labview program specifically written for this work. As an example, data for the 0.6 weight % PNIPAM concentration, containing MNPs, sample is shown in Figs. 40 (a) and (b).
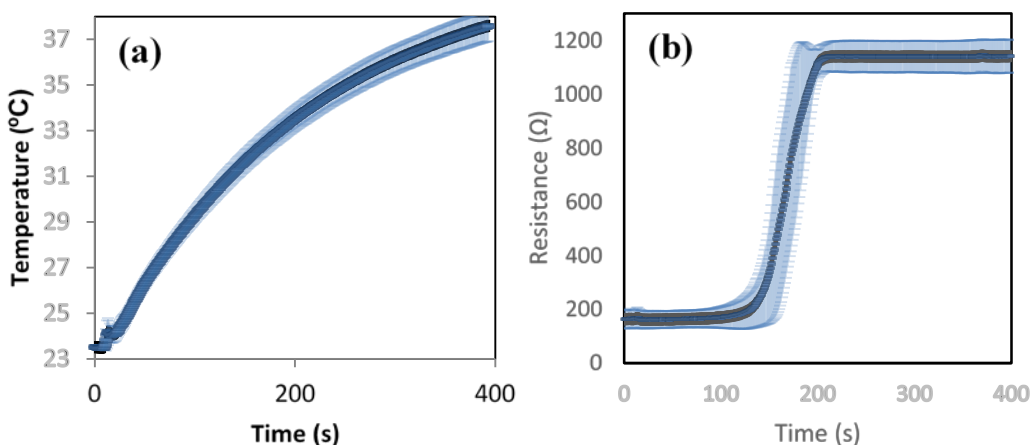

Figure 40. (a) The heating curve for a 0.6 wt % PNIPAM sample containing MNPs. (b) Resistance versus time data for a 0.6 wt % PNIPAM sample containing MNPs.

The phase transition is indicated, in Figure 41, by the abrupt change in resistance. However, it is the temperature at which the LCST occurs, not when it occurs, that is of interest. For this reason the data sets are both collected in 1 second time intervals so that the resistance data can easily be correlated to the temperature data. Also, the resistance is converted into a transmittance. The result is a transmittance percent versus temperature data set like that shown in Figure 42 (a). Once all samples have been tested and analyzed the data can be plotted on

Figure 41. Transmittance % versus temperature data indicating the LCST of a 0.6 wt % PNIPAM solution containing MNPs.

the same graph. Figure 42 (b) clearly demonstrates that the LCST can be controlled by determining the sample's concentration of PNIPAM. Note how the LCST increases with decreasing PNIPAM concentration. We can precisely identify the LCST by evaluating the derivative of the transmittance as shown in Figure 16 for three sample concentrations.
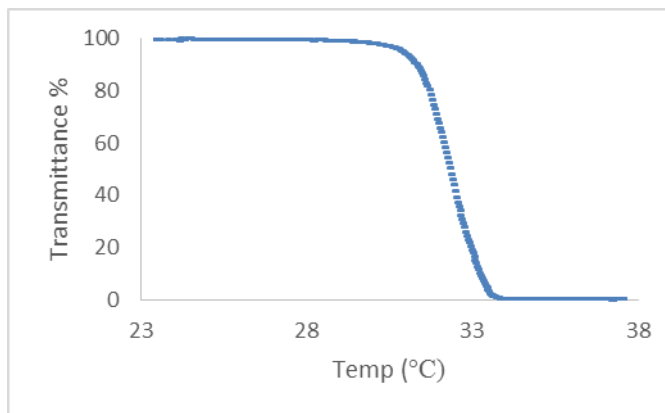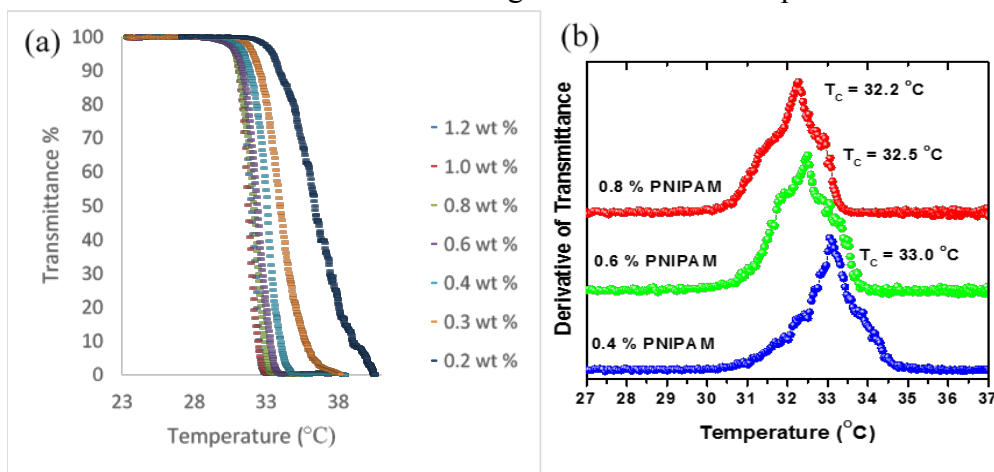

Figure 42. (a) Transmittance % vs temperature data for 1.2, 1.0, 0.8, 0.6, 0.4, 0.3, and 0.2 wt % PNIPAM containing MNPs. (b) The derivative of the transmittance versus temperature data for precise identification of the LCST.

By designing and building a setup for optical studies of PNIPAM an in-situ method for testing a drug delivery vehicle has been devised. Near-term future work will focus on investigating whether or not changing the concentration of MNPs will have any influence on the LCST of PNIPAM. Long-term future work will focus on investigating other thermo-responsive polymers such as poly(lactic glycolic acid) (PLGA) with this technique.

Systematic study on the remote triggering of thermo-responsive PNIPAM hydrogels using RF heating of magnetite nanoparticles

Thermo-responsive hydrogels such as poly-N-isopropylacrylamide (PNIPAM) exhibit reversible swelling/shrinking properties, making them ideal candidates for controlled release applications such as drug delivery.[39] For practical applications, remote triggering of the hydrogels is desired, which is realized by heating magnetic nanoparticles/hydrogels composites by exposing them to external alternating radiofrequency (RF) magnetic field [40]. Literature survey shows that a detailed study on the phase transitions in PNIPAM using remote heating of magnetite nanoparticles is absent [41-46].

In this work, we present a systematic study on the factors that influence the lower critical solution temperature (LCST) of PNIPAM hydrogels during their RF heating using Fe_3O_4 nanoparticles. Preliminary studies have shown that the highest specific absorption rate (SAR) for is achieved for 15 nm sized Fe_3O_4 nanoparticles, which monotonically decreases as the nanoparticle sizes increased to 25 nm. A series of PNIPAM solutions with varying concentrations of Fe_3O_4 nanoparticles were prepared and characterized using transmission electron microscopy (TEM), dynamic light scattering (DLS) and Raman spectroscopy. In-situ transmission measurements were used to determine the LCST of PNIPAM under various aqueous concentrations with dispersed Fe_3O_4 nanoparticles. A systematic decrease in the LCST from 34 ºC to 31 ºC is reported as the concentration of PNIPAM is increased from 0.2 wt. % to 1.2 wt. %, keeping the concentration of Fe_3O_4 nanoparticles constant. On the other hand, we observe that varying the concentrations of the nanoparticles does not drastically affect the LCSTs of PNIPAM solutions. However, increasing the basicity of the PNIPAM solutions by adding adjusted KOH pellets, show a pronounced lowering of the LCST by 2-3 ºC at all PNIPAM concentrations. The controlled remote tuning of the LCST in PNIPAM using Fe_3O_4 nanoparticles as reported here provides valuable information towards using these thermo-responsive polymers for targeted and controlled release in drug delivery. Detailed analysis of the optimized SAR of Fe_3O_4 nanoparticles and LCST of PNIPAM solutions is presented and discussed for future applications.

Aqueous solutions of high purity PNIPAM (99.99 %, Sigma-Aldrich) with a molecular weight of 10,000 ($M_n = 10,000$) and Fe_3O_4 MNPs (99.5 %, US Research Nanomaterials, Inc.) of varying sizes from 15 to 25 nm were prepared by mixing desired amounts of the powders in deionized water (DIW). Prior to transmission measurements, the Fe_3O_4 MNPs were fully dispersed in the solutions by repeated ultra-sonication for 15 mins to achieve a homogeneous distribution.
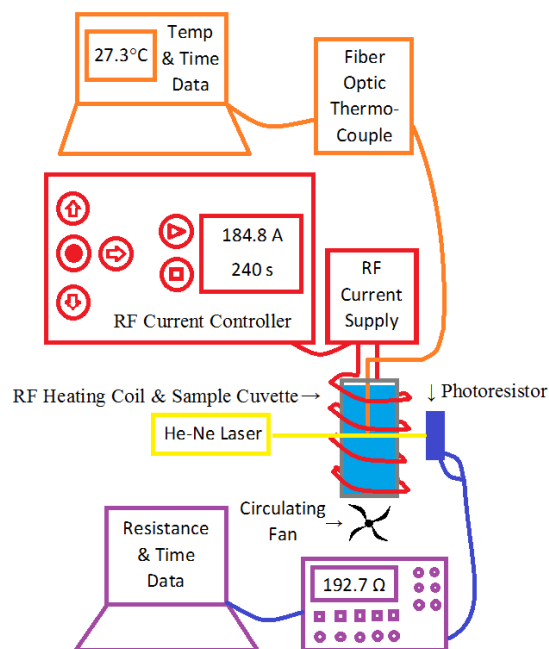

Figure 43: Experimental setup for the determination the LCST of PNIPAM aqueous samples. He-Ne laser beam is obscured by the turbidity change as the sample is heated.

Few drops of the dispersed PNIPAM/Fe$_3$O$_4$ solutions were drop-casted onto carbon-coated Cu grids for transmission electron microscope (TEM, FEI Morgani operated at 60 kV acceleration voltage) imaging. Raman spectra of the prepared solutions were acquired using a Horiba Jobin Yvon T64000 Advanced Research Raman System equipped with an argon laser operated at 514 nm. The turbidity change associated with the phase transition in the PNIPAM/Fe$_3$O$_4$ solutions was detected using transmission measurements with a 25 mW He-Ne laser (CW Radiation, Inc.) of 633 nm wavelength. For transmission measurements, the dispersed solution was transferred to an optical cuvette that was suspended in the RF heating coil (see Figure 43). The laser was aligned so as to pass between the loops of the coil and through the optical cuvette. The transmitted laser beam was incident on a cadmium-sulfide photoresistor and the change in resistance was measured as a function of time using a Keithley 2100 Multimeter and LabView programmed data acquisition. The PNIPAM/Fe$_3$O$_4$ solution within the sample cuvette were heated using an alternating magnetic field (740 Oe) at an optimum current (184.8 A) using an Ambrell EasyHeat LI heating system operating at a safe-frequency of 307 kHz. Temperature changes in the sample induced by the RF heating system were monitored by an optical temperature sensor (Photon Control) with an accuracy of +/- 0.05°C.

Effect of Fe$_3$O$_4$ MNP size and concentration on the RF heating rates and specific absorption rates for PNIPAM/Fe$_3$O$_4$ aqueous solutions

Figure 44 (a) shows the relative temperature changes (with respect to room-temperature) versus time (heating curves) of PNIPAM/Fe$_3$O$_4$ solutions with varying size of the Fe$_3$O$_4$ MNPs from 15 to 25 nm. It was observed that the most efficient heating occurs when the MNP sizes are about 15 nm, which was considered as the optimum particle size for the subsequent studies [47].
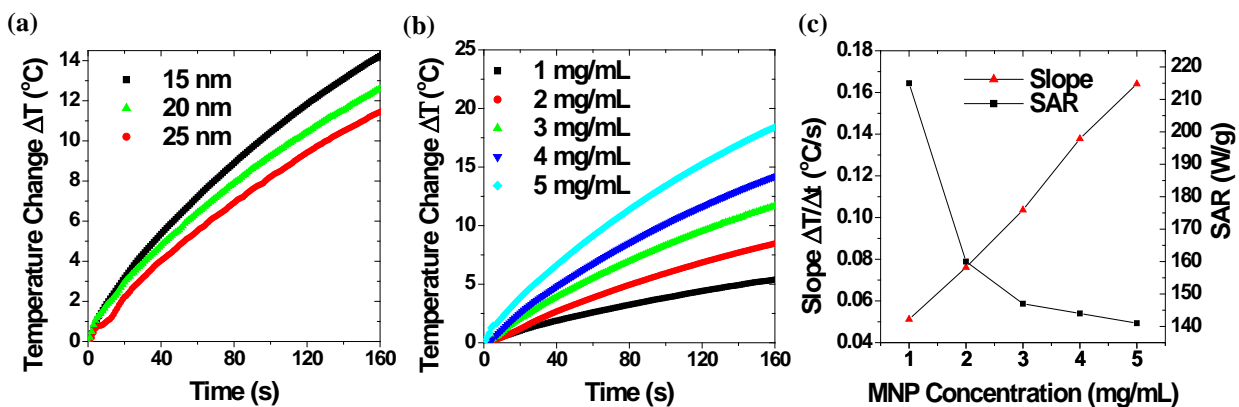

Figure 44. Optimization of RF heating using PNIPAM/Fe$_3$O$_4$ solutions with (a) varying sizes of the Fe$_3$O$_4$ MNPs from 15 to 25 nm, and (b) varying MNPs concentrations from 1 to 5 mg/mL using the optimum MNP size of 15 nm. The concentration of PNIPAM was kept constant at 0.2 wt. % throughout these experiments. (c) SAR and slope ($\Delta T/\Delta t$) were calculated as a function of MNP concentration (mg/mL) from the initial linear portions of the heating curves in figure 44 (b).

Figure 44 (b) shows the heating curves of PNIPAM/Fe$_3$O$_4$ solutions with varying concentrations of the Fe$_3$O$_4$ MNPs using the optimum MNP size of 15 nm. The rate of heating of PNIPAM/Fe$_3$O$_4$ solutions increases monotonically as the concentration of MNPs increases in the solutions, which is expected since at higher concentrations more Fe$_3$O$_4$ MNPs are available to transfer heat to the solution. The linear slope ($\Delta T/\Delta t$) of the heating curve (heating rate) was

determined from Fig. 44 (b) and plotted as a function of MNP concentration in Fig. 44 (c). With the linear slope values the specific absorption rates (SAR), also shown in Fig. 44 (c), were calculated using the following equation:

$$SAR = \frac{\sum_i c_i m_i}{m_{Fe_3O_4}} \left(\frac{\Delta T}{\Delta t}\right)$$

Here the specific heats of PNIPAM, water, and Fe_3O_4 were taken to be 1200, 4180, and 650 J/kg/°C respectively. SAR is heat energy per unit time for a unit mass. Evidently, the SAR values decrease in a non-linear fashion with increasing Fe_3O_4 MNP concentrations, while the initial slope of the heating curve increases in a linear monotonic fashion. Despite the fact that the SAR values are proportional to the slope of the linear portion of the heat curve, depicted in Fig. 44 (b), they exhibit a decreasing trend due to the mass normalization involved in their calculations. The concentration in Fig. 44 (c), where the two data sets cross was taken to be the optimum concentration of MNPs. From the above analysis, the optimum MNP concentrations were found to be 2 and 3 mg/mL while the optimum MNP size was considered to be 15 nm.

After executing several RF heating cycles, the chemical compositions of the PNIPAM/Fe_3O_4 solutions were characterized using Raman spectroscopy to ensure no thermal degradation of PNIPAM. As shown in Fig. 45 (a), the Raman spectrum of the PNIPAM remains unchanged after RF heating indicating no structural degradation with repeated heat on/off cycles. This is critical in practical applications where decomposition of the polymer under excessive RF heating could lead to complications in the desired drug delivery. Further, the presence of the Fe_3O_4 MNPs is not detected in the Raman spectrum in Fig. 45 (a). The strong Raman peaks from PNIPAM obscure the Raman spectrum of the Fe_3O_4 MNP as shown in the inset to Fig. 45 (a) (measured separately). Fig. 45 (b) shows the TEM images of the Fe_3O_4 MNPs showing indication of some agglomeration as a result of repeated RF heating.
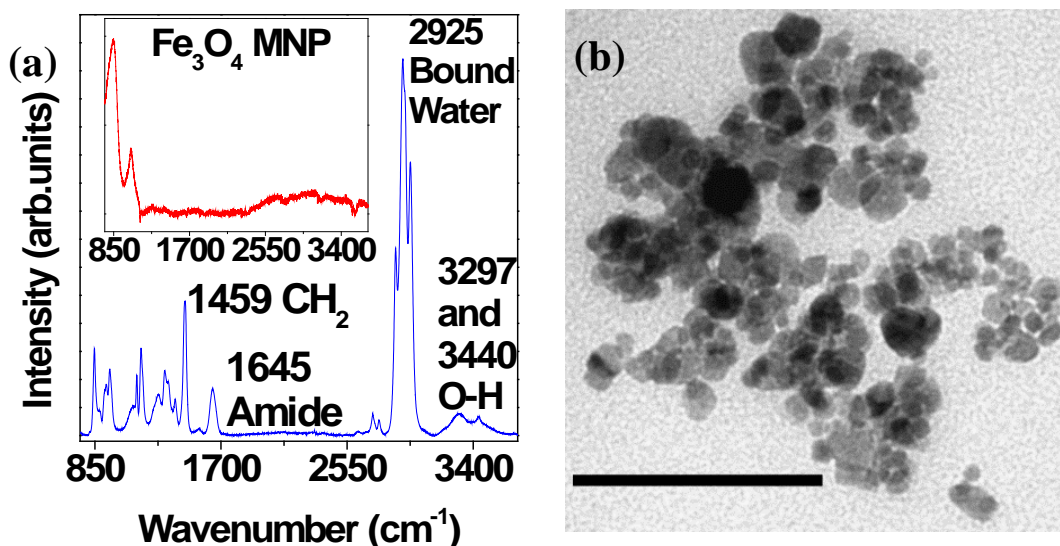

Figure 45. (a) Raman spectra of PNIPAM/Fe_3O_4 solution measured at room temperature after repeated RF heating cycles. Insert shows the Raman spectra from Fe_3O_4 MNPs. (b) TEM image of Fe_3O_4 MNPs after RF heating. The scale bar is 100 nm.

Effect of PNIPAM concentrations on the transition temperatures of PNIPAM/Fe₃O₄ aqueous solutions under RF heating conditions

Figure 46 (a) shows the temperature-dependent-transmission at wavelength of 633 nm (He-Ne laser) obtained for aqueous solutions of PNIPAM/Fe₃O₄ at various polymer concentrations ranging from 0.3 to 1.2 wt. %, keeping constant concentration of Fe₃O₄ MNPs at 2 mg/mL. From the figure it is evident that the inflection point where the transmittance fraction drops from 100 % to 0 % changes with PNIPAM concentrations. The lower critical solution temperature (LCST) for PNIPAM/Fe₃O₄ aqueous solution was taken as the temperature where the modulus of the derivative of the transmittance reaches maxima. In order to determine the LCST the derivative of the transmittance was fitted with a Gaussian function distribution, shown in Fig. 46 (b) and the maximum of the curve was taken as the transition temperature. Figure 46 (c) shows the LCST values of the PNIPAM/Fe₃O₄ aqueous solutions at different PNIPAM concentrations, keeping the Fe₃O₄ MNP concentrations constant at 2 and 3 mg/mL, respectively. A monotonic decrease in the LCST values with increasing PNIPAM concentrations is observed from Fig. 46 (c), for both concentrations of Fe₃O₄ MNPs. PNIPAM has an LCST that is concentration dependent since as the fraction of PNIPAM chains to solvent is increased in the solution, the switch from enthalpy to entropy dominance of the free energy occurs sooner. In previous works turbidimetry studies were carried out on PNIPAM solutions while heating via conduction. As in those other works, the data presented in Fig. 46 shows a LCST for PNIPAM that is polymer concentration dependent. The data in Fig. 46 matches data presented in reports for the bulk heating of PNIPAM [35]. Thus, the remote heating of PNIPAM discussed herein was successful. Furthermore, it is evident in Fig. 46 (c) that varying the concentration of MNPs does not affect the LCST of a given PNIPAM/Fe₃O₄ solution.
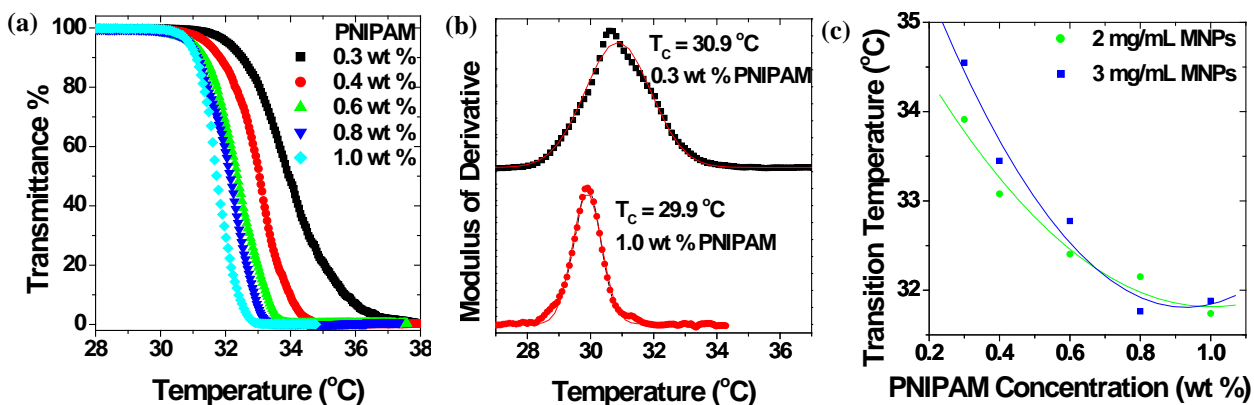

Figure 46. (a) Temperature dependence of optical transmittance at 633 nm obtained for PNIPAM/Fe₃O₄ concentrations varying as 0.3, 0.4, 0.6, 0.8, and 1.0 wt %, with constant Fe₃O₄ MNPs concentration of 2 mg/mL Fe₃O₄ MNPs. (b) Modulus of derivative of transmittance as a function of temperature for 0.3 and 1.0 wt % PNIPAM. (c) Transition temperature (LCST) versus polymer concentration of PNIPAM/Fe₃O₄ aqueous solutions in which the MNP concentrations are 2 and 3 mg/mL.

Effect of adding the salt KOH to PNIPAM/Fe₃O₄ aqueous solutions on the LCST

The effect of adding salt to introduce ions to the PNIPAM/Fe₃O₄ aqueous solutions was also studied. Enough KOH was added to the solvent to give it a molar concentration of 0.10 M. Figure 47 (a) shows the temperature-dependence of light transmittance for different concentrations of aqueous polymer solutions with added KOH. It is evident, from Fig. 47 (b) that

increasing the molar concentration of KOH in PNIPAM/Fe$_3$O$_4$ aqueous solutions drastically decreases the LCST values of PNIPAM/Fe$_3$O$_4$ aqueous solutions.
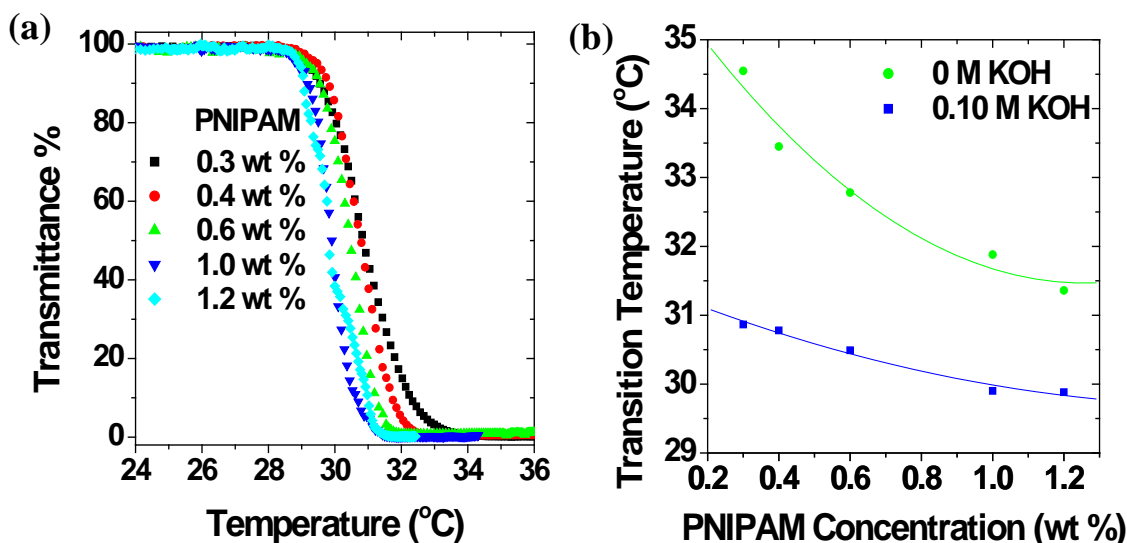

Figure 47. (a) Temperature dependence of optical transmittance at 633 nm obtained for PNIPAM/Fe$_3$O$_4$ aqueous solutions with added KOH and varying polymer concentrations between 0.3, 0.4, 0.6, 1.0, and 1.2 wt %, with constant Fe$_3$O$_4$ MNPs concentration of 3 mg/mL. (b) Transition temperature (LCST) versus polymer concentration of PNIPAM/Fe$_3$O$_4$, with constant MNP concentration 3 mg/mL, aqueous solutions with and without KOH.

It has been found that increasing KOH concentration, for example, will linearly decrease the LCST. This is understood in terms of the added ion's effect on the interaction of the solvent with the polymer. The hydroxide ion, through its electric field, arranges water molecules around the PNIPAM in such a way so as to increase the entropy of the entire system. Since the free energy of the system is dominated by entropy earlier, as compared to the case without added salt, the phase transition occurs at a lower temperature.

In conclusion, the remote triggering of PNIPAM/Fe$_3$O$_4$ aqueous solutions using RF heating with Fe$_3$O$_4$ MNPs was successfully demonstrated. The highest specific absorption rate (SAR) was achieved for 15 nm sized Fe$_3$O$_4$ MNPs, which monotonically decreased as the MNP sizes increased to 25 nm. In-situ transmission measurements showed that the LCST of PNIPAM/Fe$_3$O$_4$ aqueous solutions under various polymer concentrations decreased systematically from 34 ºC to 31 ºC as the concentration of PNIPAM was increased from 0.2 wt. % to 1.2 wt. %, keeping the concentration of Fe$_3$O$_4$ MNPs constant. On the other hand, varying the concentrations of the MNPs did not drastically affect the LCSTs of PNIPAM solutions. Increasing the ion concentration of the PNIPAM solutions by adding adjusted KOH pellets, showed a pronounced lowering of the LCST by 2-3 ºC at all PNIPAM concentrations. The controlled remote tuning of the LCST in PNIPAM using Fe$_3$O$_4$ MNPs as reported here will be of interest to researchers studying the use of these thermo-responsive polymers for targeted and controlled release in drug delivery.

III. Reportable Outcomes

Journal Publications:

1. "Intrinsic Anomalous Ferroelectricity in Vertically-Aligned $LiNbO_3$-type $ZnSnO_3$ Hybrid Nanoparticle-Nanowire Arrays", **D. Mukherjee**, A. Datta, C. Kons, *M. Hordagoda*, **S. Witanachchi** and **P. Mukherjee**, *Applied Physics Letters,* 2014. (*accepted*)

2. "Evidence of Superior Ferroelectricity in Structurally Welded $ZnSnO_3$ Nanowire Arrays", A. Datta, **D. Mukherjee**, C. Kons, **S. Witanachchi** and **P. Mukherjee**, *Small* **10**, 4093 (2014).

3. "On-the-surface photoconductive response of pelletized thin In_2S_3 nanosheets", A. Datta, **D. Mukherjee**, **S. Witanachchi** and **P. Mukherjee**, *Materials Research Bulletin*, **55**, 176-181 (2014).

4. "Hierarchically-Ordered Nano-Heterostructured PZT Thin Films with Enhanced Ferroelectric Properties", A. Datta, **D. Mukherjee**, **S. Witanachchi** and **P. Mukherjee**, *Advanced Functional Materials* **24**, 2638-2647 (2014).

5. "Enhanced magnetism and ferroelectricity in epitaxial $Pb(Zr_{0.52}Ti_{0.48})O_3$ /$CoFe_2O_4$ / $La_{0.7}Sr_{0.3}MnO_3$ multiferroic heterostructures grown using dual-laser ablation technique", **D. Mukherjee**, *M. Hordagoda*, P. Lampen, **M. H. Phan**, **H. Srikanth**, **S. Witanachchi**, and **P. Mukherjee**, *Journal of Applied Physics* **115**, 17D707 (2014).

6. "Enhanced Magnetism in Highly Ordered Magnetite Nanoparticle-filled Nanohole Arrays" - B. Duong, **H. Khurshid**, P. Gangopadhyay, *J. Devkota*, *K. Stojak*, **H. Srikanth**, L. Tetard, R. Norwood, N. Peyghambarian, **M.H. Phan**, and J. Thomas, *Small* **10**, 2840 (2014)

7. "Tuning Exchange Bias in $Fe/\gamma Fe_2O_3$ Core-Shell Nanoparticles: Impacts of Interfacial Frozen and Surface Spins" - **H. Khurshid**, **M.H. Phan**, **P. Mukherjee**, **H. Srikanth**, *Applied Physics Letters* **104**, 072407 (2014)

8. "Synthesis, inductive heating, and magnetoimpedance-based detection of multifunctional Fe_3O_4 nanoconjugates" *J. Devkota*, T.T.T. Mai, *K. Stojak*, P.T. Ha, H.N. Pham, X.P. Nguyen, **P. Mukherjee**, **H. Srikanth**, and **M.H. Phan**, *Sensors and Actuators B: Chemical* 190, 715 (2014)

9. "Exchange bias effect in $Au-Fe_3O_4$ Composite Nanoparticles" - *S. Chandra*, N. A. Frey, **M.H. Phan**, S. Srinath, Y. Lee, C. Wang, S. Sun, M. A. Garcia, and **H. Srikanth,** *Nanotechnology* 25, 055702 (2014)

10. "Magneto-impedance Based Probe of Various Concentrations of Corrosive Chemicals" - *J. Devkota*, N.T. Huong, **H. Srikanth**, and **M.H. Phan**, *IEEE Transactions on Magnetics* **50**, 4004404 (2014)

11. "Impact of coating amorphous and crystalline cobalt ferrite films on the magneto-impedance response of a soft ferromagnetic amorphous ribbon," **D. Mukherjee**, *J. Devkota*, *A. Ruiz*, **S.**

Witanachchi, P. Mukherjee, H. Srikanth, and **M.H. Phan,** *Journal of Applied Physics* **116**, 123912 (2014)

12. "A highly sensitive magnetic biosensor for detection and quantification of anticancer drugs tagged to superparamagnetic nanoparticles" - *J. Devkota*, *J. Wingo*, T. T. T. Mai, X. P. Nguyen, N. T. Huong, **P. Mukherjee**, **H. Srikanth**, and **M.H. Phan**, *Journal of Applied Physics* **115**, 17B503 (2014)

13. "Tailoring magnetic and microwave absorption properties of glass-coated soft ferromagnetic amorphous microwires for microwave energy sensing" - *J. Devkota*, P. Colosimo, A. Chen, V.S. Larin, **H. Srikanth**, and **M.H. Phan,** *Journal of Applied Physics* **115**, 17A525 (2014)

14. "Impacts of surface spins and inter-particle interactions on the magnetism of hollow γ-Fe$_2$O$_3$ nanoparticles" - **H. Khurshid**, *Z. N. Porshokouh*, **M.H. Phan**, **P. Mukherjee**, and **H. Srikanth**, *Journal of Applied Physics* **115**, 17E131 (2014)

15. "Sensing RF and microwave energy with fiber Bragg grating heating via soft ferromagnetic glass-coated microwires" - P. Colosimo and A. Chen, *J. Devkota*, **H. Srikanth**, and **M.H. Phan**, *Sensors and Actuators A: Physical* **210**, 25 (2014)

16. "Magneto-reactance based detection of MnO nanoparticle-embedded Lewis lung carcinoma cancer cells," *J. Devkota*, M. Howell, S. Mohapatra, **P. Mukherjee**, **H. Srikanth**, **M.H. Phan**,
Journal of Applied Physics (2014, in press)

17. "A soft ferromagnetic multiwire-based inductance coil sensor for advanced sensing applications" - *J. Devkota*, L. Trang, J. Liu, F. Qin, J. Sun, **P. Mukherjee**, **H. Srikanth**, and **M.H. Phan**, *Journal of Applied Physics* (2014, to be published)

18. "Superparamagnetic properties of carbon nanotubes filled with NiFe$_2$O$_4$ nanoparticles" - *K. Stojak Repa*, J. Alonso, **M.H. Phan**, **H. Srikanth**, E. M. Palmero, M. Vazquez, *Journal of Applied Physics* (2014, in press)

19. "From core-shell to hollow Fe/γ-Fe$_2$O$_3$ nanoparticles: evolution of the magnetic behavior", *Z. Nemati*, **H. Khurshid**, **J. Alonso**, **M.H. Phan**, **P. Mukherjee**, **H. Srikanth**, *Physics Review B* (2014, to be submitted)

Conference Presentations

1. "Magneto-reactance based detection of MnO nanoparticle-embedded Lewis lung carcinoma cancer cells," (poster) *J. Devkota*, M. Howell, S. Mohapatra, **P. Mukherjee**, **H. Srikanth**, and **M.H. Phan**, 59th annual conference on Magnetism and Magnetic Materials (MMM), Honolulu, Hawaii, (Nov. 3-7, 2014).

2. "Manipulating specific absorption rate of iron oxide nanoparticles by modifying shape anisotropy," (oral) ***H. Khurshid***, *J. Alonso*, *Z. Nemati*, **M.H. Phan**, **P. Mukherjee**, M. L. Fdez-Gubieda, J. M. Barandiarán, and **H. Srikanth,** 59th annual conference on Magnetism and Magnetic Materials (MMM), Honolulu, Hawaii, (Nov. 3-7, 2014).

3. "FeCo nanowires for enhanced magnetic hyperthermia," (poster) ***J. Alonso***, *H. Khurshid*, *V. Sankar*, *Z. Nemati*, **M.H. Phan**, E. Garayo, J.A. García, and **H. Srikanth,** 59th annual

conference on Magnetism and Magnetic Materials (MMM), Honolulu, Hawaii, (Nov. 3-7, 2014).

4. "Superparamagnetic properties of carbon nanotubes filled with $NiFe_2O_4$ nanoparticles," (poster) *K. Stojak Repa*, *D. Israel*, ***J. Alonso***, **M.H. Phan**, E.M. Palmero, M. Vazquez, and **H. Srikanth,** 59th annual conference on Magnetism and Magnetic Materials (MMM), Honolulu, Hawaii, (Nov. 3-7, 2014).

5. "From core-shell to hollow $Fe/\gamma-Fe_2O_3$ nanoparticles: evolution of the magnetic behavior" – *Z. Nemati*, **H. Khurshid**, ***J. Alonso***, **M.H. Phan**, and **H. Srikanth,** 59th annual conference on Magnetism and Magnetic Materials (MMM), Honolulu, Hawaii, (Nov. 3-7, 2014).

6. "Magnetic characteristics of Strain Modified $CoFe_2O_4$ Thin Films in $La_{0.7}Sr_{0.3}MnO_3/BaTiO_3/CoFe_2O_4$ Multiferroic Heterostructures", *M. Hordagoda*, **D. Mukherjee**, **M. H. Phan**, **H. Srikanth**, **S. Witanachchi**, and **P. Mukherjee**, Materials Research Society, 2014 MRS Spring Meeting & Exhibit, San Francisco, CA (April 21st - 25th, 2014).

7. "The Effect of Very Low Doping Concentrations of La in La Doped PZT Thin Films", *M. Hordagoda*, **D. Mukherjee**, **P. Mukherjee**, and **S. Witanachchi**, Materials Research Society, 2014 MRS Spring Meeting & Exhibit, San Francisco, CA (April 21st - 25th, 2014).

8. "Enhanced surface-quality, magnetic and ferroelectric properties in epitaxial PZT/LSMO multiferroic heterostructures grown using dual-laser ablation", **D. Mukherjee**, *M. Hordagoda*, **H. Srikanth**, **S. Witanachchi**, and **P. Mukherjee**, American Ceramic Society, 38th International Conference and Exposition on Advanced Ceramics and Composites, Daytona Beach, FL (Jan. 26th-31st, 2014) (invited).

9. "Physical/Chemical Combinatorial Strategy Towards Multi-dimensional Perovskite Nano- and Micro-structures with Enhanced Functionality", A. Datta, **D. Mukherjee**, **S. Witanachchi**, and **P. Mukherjee**, American Ceramic Society, 38th International Conference and Exposition on Advanced Ceramics and Composites, Daytona Beach, FL (Jan. 26th-31st, 2014) (invited).

10. "Role of dilute La-doping in enhancing the polarization in epitaxial $Pb1-xLaxZr_{0.52}Ti_{0.48}O_3$ thin films", *M. Hordagoda*, **D. Mukherjee**, D. Ghosh, J. L. Jones, **S. Witanachchi**, and **P. Mukherjee**, American Ceramic Society, 38th International Conference and Exposition on Advanced Ceramics and Composites, Daytona Beach, FL (Jan. 26th-31st, 2014).

11. "Magnetic and ferroelectric property enhancement of PZT/LSMO multiferroic thin films using dual laser ablation", *M. Hordagoda*, **D. Mukherjee**, R.Hyde, **P. Mukherjee**, and **S. Witanachchi**, American Ceramic Society, Electronic Materials and Applications 2014, Orlando, FL (Jan. 22nd-24th, 2014).

12. "The effect of La doping on the ferroelectric and magnetic properties of PZT/LSMO multiferroic heterostructures", *M. Hordagoda*, **D. Mukherjee**, D. Ghosh, J. L. Jones, **P. Mukherjee**, and **S. Witanachchi**, American Ceramic Society, Electronic Materials and Applications 2014, Orlando, FL (Jan. 22nd-24th, 2014).

13. "Enhanced ferroelectric properties in epitaxial La-doped PZT films at low concentrations of La-doping", *M. Hordagoda*, **D. Mukherjee**, D. Ghosh, J. L. Jones, **P. Mukherjee**, and **S.**

Witanachchi, American Ceramic Society, Electronic Materials and Applications 2014, Orlando, FL (Jan. 22nd-24th, 2014).

14. "Controlled seed-layer assisted growth of hierarchically-ordered $PbZr_{0.52}Ti_{0.48}O_3$ nanostructure arrays with improved ferroelectric properties", A. Datta, **D. Mukherjee**, **S. Witanachchi**, and **P. Mukherjee**, American Ceramic Society, 38th International Conference and Exposition on Advanced Ceramics and Composites, Daytona Beach, FL (Jan. 26th-31st, 2014).

15. "Static and dynamic properties of hollow and spherical γ-Fe_2O_3 nanoparticles" (poster) –**H. Khurshid**, *S. Chandra*, **M.H. Phan, P. Mukherjee** and **H. Srikanth**

16. "Tuning exchange bias in core-shell Fe/ Fe$_2$O$_3$ nanoparticles: role of frozen interfacial and surface spins" (poster) –**H. Khurshid**, **M. Phan, P. Mukherjee** and **H. Srikanth**

17. "Synthesis, inductive heating and magneto-impedance based detection of multi-functional Fe_3O_4 nanoconjugates" (poster) –*J. Devkota, K. Stojak, J. Wingo*, T. T. Mai, P. T. Ha, H. N. Pham, X. P. Nguyen, **P. Mukherjee, H. Srikanth** and **M. H. Phan**

18. "Tailoring magnetic and microwave absorption properties of glass-coated soft magnetic microwires for microwave energy sensing applications" (oral) –*J. Devkota*, P. Colosimo, *J. Wingo*, A. Chen, **H. Srikanth** and **M. H. Phan**, 58th annual conference on Magnetism and Magnetic Materials (MMM), Denver, CO (Nov. 4-8, 2013).

19. "Static and dynamic properties of hollow and spherical γ-Fe_2O_3 nanoparticles" (poster) –**H. Khurshid**, *S. Chandra*, **M.H. Phan, P. Mukherjee** and **H. Srikanth**, 58th annual conference on Magnetism and Magnetic Materials (MMM), Denver, CO (Nov. 4-8, 2013).

20. "Tuning exchange bias in core-shell Fe/γ-Fe_2O_3 nanoparticles: role of frozen interfacial and surface spins" (poster) –**H. Khurshid**, **M. Phan, P. Mukherjee** and **H. Srikanth,** 58th annual conference on Magnetism and Magnetic Materials (MMM), Denver, CO (Nov. 4-8, 2013).

21. "Synthesis, inductive heating and magneto-impedance based detection of multi-functional Fe_3O_4 nanoconjugates" (poster) –*J. Devkota, K. Stojak, J. Wingo*, T. T. Mai, P. T. Ha, H. N. Pham, X. P. Nguyen, **P. Mukherjee, H. Srikanth** and **M. H. Phan,** 58th annual conference on Magnetism and Magnetic Materials (MMM), Denver, CO (Nov. 4-8, 2013).

22. "Tailoring magnetic and microwave absorption properties of glass-coated soft magnetic microwires for microwave energy sensing applications" (oral) –*J. Devkota*, P. Colosimo, *J. Wingo*, A. Chen, **H. Srikanth** and **M. H. Phan,** 58th annual conference on Magnetism and Magnetic Materials (MMM), Denver, CO (Nov. 4-8, 2013).

Book Chapter:

- "Laser Ablation for Multiferroic Heterostructures", **D. Mukherjee**, **S. Witanachchi**, and **P. Mukherjee**, in *Laser Ablation: Fundamentals, Methods and Applications*, NOVA Publishers (in press).

Major presentations:

- "Exchange bias and novel phenomena in hybrid nanostructures" –Invited talk (**Hari Srikanth**), Donostia International Conference on Nanoscaled Magnetism and Applications, San Sebastian (SPAIN), September 9-13, 2013

- "Tunable exchange bias in core-shell and coupled nanoparticles" –Invited talk (**Hari Srikanth**), Magnetic Materials and Applications (MagMA-2013) conference, Guwahati (INDIA), December 5-7, 2013

- "Magneto-impedance based detection of magnetic biomarkers: Opportunities and Challenges" Invited Talk (**M.H. Phan**) at the Energy Materials Nanotechnology (EMN) Fall Meeting, December 7 – 10, 2013 Orlando, Florida, USA

- "Functional nanoparticles for energy and nanomedicine applications" - Invited talk (**Hari Srikanth**), Nano and Giga challenges in Electronics, Photonics and Renewable Energy symposium 2014, Arizona State University, Phoenix, AZ (March 2014)

- "Hybrid nanoparticles for hyperthermia and biosensing applications," – Invited talk (**Hari Srikanth**), Zing Bionanomaterials Conference, Nerja (Spain), April 2014

- Seminar at Slovak Academy of Sciences "Functional Magnetic Nanostructures" - Invited talk (**Hari Srikanth**), Kosice, Slovak Republic (July 1, 2014)

- "Magnetic nanostructures for microwave devices and biosensors," Invited talk (**Hari Srikanth**), European Magnetic Sensors and Actuators (EMSA) conference, Vienna, Austria (July 6-9, 2014)

- "Advanced magnetoimpedance based biosensing using functionalized nanoparticles," Invited Talk (**M.H. Phan**) at the 59th Annual Magnetism and Magnetic Materials (MMM) Conference, November 3-7, 2014, Hawaii, USA

IV. Conclusions

The following sub-tasks under Task I are being pursued through the no-cost extension of the continuation grant:

1. Synthesis of PEG, Dextran-coated nanoparticles and clusters for hyperthermia experiments and their structural and magnetic characterization.
2. Measurements and comparative analysis of specific absorption rates and AC power losses of ferrofluids for magnetic hyperthermia applications.
3. *Magnetoimpedance measurements and sensing of biomolecules.*
4. Formation and delivery of functionalized artificial platelets for rapid cessation of internal bleeding.

Specifically, during the past year the following sub-tasks and projects were completed:

Nanostructured materials for biomedical diagnostics and chemical sensing

A. Inductive heating (hyperthermia) studies on novel magnetic nanostructures
  1. Iron oxide nanoparticles with controlled morphology for magnetic hyperthermia
  2. Novel exchange-coupled FeO/Fe$_3$O$_4$ nanoparticles for magnetic hyperthermia
  3. Novel FeCo nanowires with enhanced heating powers for magnetic hyperthermia

B. High aspect-ratio magnetic nanostructures for novel biosensors and microwave device applications
  1. Superparamagnetic properties of carbon nanotubes filled with NiFe$_2$O$_4$ nanoparticles
  2. Enhanced magnetic properties of carbon nanotubes filled with core/shell Fe/γFe$_2$O$_3$ nanoparticles
  3. Highly ordered magnetite nanoparticle-filled nanohole arrays for biomedical applications

C. Soft ferromagnetic materials and magneto-impedance technology for microwave energy, chemical and biological sensing
  1. Glass-coated soft ferromagnetic amorphous microwires for microwave energy sensing
  2. A new type of multiwire-based sensors for magnetic sensing applications:
  3. A new type of magneto-reactance based biosensor for detection of cancer cells and biomolecules

Formation and delivery of functionalized artificial platelets for rapid cessation of internal bleeding

- Proposal of poly(N-isopropylacrylamide) as a polymeric drug delivery nanocapsule
- Design of the platelet delivery system
- Investigation of the transition temperature of poly (N-isopropylacrylamide)
  o RF heating of DIW
  o RF heating of MNPs and DIW
  o RF heating of PNIPAM, MNPs, and DIW
- Systematic study on the remote triggering of thermo-responsive PNIPAM hydrogels using RF heating of magnetite nanoparticles

- Effect of Fe_3O_4 MNP size and concentration on the RF heating rates and specific absorption rates for PNIPAM/Fe_3O_4 aqueous solutions
- Effect of PNIPAM concentrations on the transition temperatures of PNIPAM/Fe_3O_4 aqueous solutions under RF heating conditions
- Effect of adding the salt KOH to PNIPAM/Fe_3O_4 aqueous solutions on the LCST

These sub-tasks will permit us to continue interdisciplinary work on research for the development of artificial platelets for delivery to promote coagulation at wound sites. This work will rely on advances already made in designed magnetic nanoparticles and physical techniques for the fabrication of polymeric micro- and nano-structures. Supporting work on related magnetic nanostructures will also continue as indicated above. Any further advances during the no-cost extension period in areas of research that have already accomplished program goals will also be reported.

V. References

1. D. Ortega and Q.A. Pankhurst *Magnetic hyperthermia Nanostructures Through Chemistry* (Nanoscience vol. 1) (Cambridge: The Royal Society of Chemistry) p 60 (2013)

2. Q.A. Pankhurst, J. Connolly, S.K. Jones and J. Dobson, J. Phys. D: Appl. Phys. 36, R167 (2003).

3. M. Suto, Y. Hirota, H. Mamiya, A. Fujita, R. Kasuya, K. Tohji, and B. Jeyadevan. J. Mag. Mag. Mat. 321(10), 1493 (2009).

4. H. Khurshid, S. Chandra, W. Li, G. C. Hadjipnayis, P. Mukherjee, M. H. Phan, and H. Srikanth, J. Appl. Phys. 113, 17B508 (2013).

5. H. Khurshid, S. Chandra, W. Li, G. C. Hadjipnayis, P. Mukherjee, M.H. Phan, and H. Srikanth, Nanoscale 5, 7942 (2013).

6. C Vazquez-Vazquez et al., Journal of Nanoparticle Research13, 1163 (2010)

7. N. S. Akulov, Z. Physik 69, 822 (1931).

8. O. Iglesias, A. Labarta, and X. Batlle, J. Nanosci. Nanotech. 8, 2761 (2008).

9. P. Poddar, J.L. Wilson, H. Srikanth, D.F. Farrell, and S.A. Majetich Phys. Rev. B 68 214409 (2003)

10. S. Chandra, H. Khurshid, M.-H. Phan, and H. Srikanth, Appl. Phys. Lett. 101, 232405 (2012)

11. A. H. Habib, C. L. Ondeck, P. Chaudhary, M.R. Bockstaller and M. E. McHenry. J. Appl. Phys. 103, 07A307 (2008)

12. C. L. Ondeck, A. H. Habib, P. Ohodnicki, K. Miller, C. A. Sawyer, P. Chaudhary, and M. E. McHenry. J. Appl. Phys. 105, 07B324 (2009)

13. C. Martínez-Boubeta, K. Simeonidis, A. Makridis, M. Angelakeris, O. Iglesias, P. Guardia, A. Cabot, Ll. Yedra, S. Estradé, F. Peiró, Z. Saghi, P.A. Midgley, I. Conde-Leborán, D. Serantes and D. Baldomir, Scientific Reports 3, 1652 (2012).

14. J. Gass, P. Poddar, J. Almand, S. Srinath and H. Srikanth, Adv. Funct. Mater. 16, 71 (2006).

15. C. Morales, J. Dewdney, S. Susmita, S. Skidmore, K. Stojak, H. Srikanth, T. Weller and J. Wang, IEEE 1, 1340 (2010).

16. S. Pal, S. Chandra, M. H. Phan, P. Mukherjee and H. Srikanth, Nanotech. 20, 485604 (2009).

17. D. Sarkar, A. Bhattacharya, P. Nandy, S. Das, Mater. Lett. 120, 259 (2014).

18. R.K. Srivastava, T.N. Narayanan, A.P. Reena Mary, M.R. Anantharaman, A. Srivastava, R. Vajtai, P.M. Ajayan, Appl. Phys. Lett. 99, 113116 (2011).

19. M. Abdel Salam, M.A. Gabal, A.Y. Obaid, Synth. Met. 161, 2651 (2012).

20. H. Khurshid, P. Mukherjee, M. H. Phan, and H. Srikanth, Appl. Phys. Lett. 104, 072407 (2014)

21. Korneva et al., Nano Lett. 5, 879 (2005)

22. Duong et al. ACS Appl. Mater. Interfaces 5, 3894 (2013)

23. T. M. Nocera , J. Chen , C. B. Murray , G. Agarwal , Nanotechnology 23, 495704 (2012)

24. M.H. Phan and H.X. Peng, Prog. Mater. Sci. 53, 323 (2008).

25. P. Colosimo and A. Chen, J. Devkota, H. Srikanth, and M.H. Phan, Sensors and Actuators A: Physical 210, 25 (2014)

26. D. He and M. Shiwa, Sensors 14, 10644 (2014)

27. G. V. Kurlyandskaya, M. L. Sánchez, B. Hernando, V. M. Prida, P. Gorria, and M. Tejedor, Appl. Phys. Lett. 82, 3053 (2003)

28. J. Devkota, C. Wang, A. Ruiz, S. Mohapatra, P. Mukherjee, H. Srikanth, and M. Phan, J. Appl. Phys. 113, 104701 (2013).

29. J. Devkota, A. Ruiz, P. Mukherjee, H. Srikanth, and M.-H. Phan, Magnetics, IEEE Transactions on 49, 4060 (2013).

30. J. Devkota, J. Wingo, T. T. T. Mai, X. P. Nguyen, N. T. Huong, P. Mukherjee, H. Srikanth, and M. H. Phan, J. Appl. Phys. 115, 17B503 (2014)

31. M. Howell, J. Mallela, C. Wang, S. Ravi, S. Dixit, U. Garapati, and S. Mohapatra, J. Control. Release 167, 210 (2013)

32. J. P. Bertram, C. A. Williams, R. Robinson, S. S. Segal, N. T. Flynn, and E. B. Lavik, "Intravenous Hemostat: Nanotechnology to Halt Bleeding", Sci. Transl. Med. 1, 11-22 (2009).

33. A. Pich, S. Bhattacharya, A. Ghosh, and H. –J.P. Adler, "Composite magnetic particles: 2. Encapsulation of iron oxide by surfactant-free polymerization", Polymer 46, 4596-4603 (2005).

34. M. M. Yallapu, M. K. Reddy, and V. Labhasetwar, "Nanogels: Chemistry to Drug Delivery", John Wiley & Sons, 145-147 (2007).

35. M.R. Aguilar, C. Elvira, A. Gallardo, B. Vazquez, and J.S. Roman. Smart Polymers and Their Applications as Biomaterials. Topics in Tissue Engineering 2007; 3: 2-17

36. Z. Ahmed, E.A. Gooding, K.V. Pimenov, L. Wang, and S.A. Asher. UV Resonance Raman Determination of Molecular Mechansim of Poly(N-isopropylacrylamide) Volume Phase Transition 2009; 113: 4248-4256

37. W.D. Callister, D.G. Rethwisch. Materials Science and Engineering an Introduction. 2010; 14: 532-561

38. F. Meunier, A. Elaissari, and C. Pichot. Preparation and Characterization of Cationic Poly(n-Isopropylacrylamide) Copolymer Latexes. Polymer for Advanced Technologies 1995; 6: 489-496.

39. D. Schmaljohann, Adv. Drug Delivery Rev. 58, 1655–1670 (2006).

40. L. B. Chen, F. Zhang and C. C. Wang, Small 5, 621–628 (2009).

41. S. K. Sahoo, T. K. De, P. K. Ghosh, and A. Maitra, J. Colloid Inter. Sci. 206, 361-368 (1998).

42. M. Shibayama, and T. Tanaka, Adv. Polymer Sci. 109, 1-62 (1993).

43. C. Binns, Magnetic Nanoparticle Hyperthermia Treatment of Tumours in Nanostructured Materials for Magnetoelectronics, ed. by B. Atkas, F. Mikailzade (Springer, Berlin, 2013).

44. G. Vallejo-Fernandez, O. Whear, A. G. Roca, S. Hussain, J. Timmis, V. Patel and K. O'Grady, J. Phys. D: Appl. Phys. 46, 312001 (2013).

45. Q. A. Pankhurst, J. Connolly, S. K. Jones and J. Dobson, J. Phys. D: Appl. Phys. 36, R167-R181 (2003).

46. S. D. Kong, M. Sartor, C. J. Hu, W. Zhang, L. Zhang, and S. Jin, Acta Biomaterialia 9, 5447-5452 (2013).

47. C. Binns, "Magnetic Nanoparticle Hyperthermia Treatment of Tumours," in *Nanostructured Materials for Magnetoelectronics*, ed. B. Atkas, F. Mikailzade (Springer, Berlin, 2013) pp.199-212.